

Banner appropriate to article type will appear here in typeset article

# Aerodynamic equilibria and flight stability of plates at intermediate Reynolds numbers

Olivia Pomerenk<sup>1</sup> and Leif Ristroph<sup>1</sup>†

<sup>1</sup>Courant Institute of Mathematical Sciences, Applied Math Lab, New York University, New York, NY 10012

(Received xx; revised xx; accepted xx)

The passive flight of a thin wing or plate is an archetypal problem in flow-structure interactions at intermediate Reynolds numbers. This seemingly simple aerodynamic system displays an impressive variety of steady and unsteady motions that are familiar from fluttering leaves, tumbling seeds and gliding paper planes. Here, we explore the space of flight behaviors using a nonlinear dynamical model rooted in a quasi-steady description of the fluid forces. Efficient characterization is achieved by identification of the key dimensionless parameters, assessment of the steady equilibrium states, and linear analysis of their stability. The structure and organization of the stable and unstable flight equilibria proves to be complex, and seemingly related factors such as mass and buoyancy-corrected weight play distinct roles in determining the eventual flight patterns. The nonlinear model successfully reproduces previously documented unsteady states such as fluttering and tumbling while also predicting new types of motions, and the linear analysis accurately accounts for the stability of steady states such as gliding and diving. While the conditions for dynamic stability seem to lack tidy formulas that apply universally, we identify relations that hold in certain regimes and which offer mechanistic interpretations. The generality of the model and the richness of its solution space suggest implications for small-scale aerodynamics and related applications in biological and robotic flight.

**Key words:** aerodynamic modeling | unsteady aerodynamics | passive flight | flight dynamics | flow-structure interaction

## 1. Introduction

Thin structures falling through fluids exhibit a wide variety of unsteady and steady motions such as fluttering, tumbling, and gliding. Such passive flight systems are canonical areas of study for aerodynamics at intermediate Reynolds numbers ( $Re$ ) and the interactions of bodies with unsteady flows. Attempts to identify and categorize flight behaviors and understand their physical origins date back to Maxwell's discussions about the tumbling of a thin card or sheet dropped in air (Maxwell 1854). Over recent decades, work on the so-called falling paper problem has greatly intensified due to interest in related forms of

† Email address for correspondence: ristroph@cims.nyu.edu

**Abstract must not spill onto p.2**

biological locomotion (Dickinson *et al.* 1999; Walker 2002; Bergou *et al.* 2010; Ristroph *et al.* 2011; Wang 2016). The aerodynamics of thin wings and plates undergoing unsteady motions has been interrogated by many methods, including direct numerical simulations via computational fluid dynamics (Sun & Tang 2002; Pesavento & Wang 2004; Wang *et al.* 2004; Andersen *et al.* 2005*b*), laboratory experimentation (Birch & Dickinson 2003; Sane & Dickinson 2001; Andersen *et al.* 2005*b*; Dickson & Dickinson 2004; Huang *et al.* 2013; Li *et al.* 2022), and mathematical modeling (Sane & Dickinson 2002; Birch & Dickinson 2003; Dickson & Dickinson 2004; Andersen *et al.* 2005*a,b*; Pesavento 2006; Hu & Wang 2014; Nakata *et al.* 2015; Li *et al.* 2022). These and related studies have sought to characterize force generation mechanisms unique to the flight regime, such as the effect of leading edge vorticity and its shedding during wing translation as well as lift modifications due to pitching rotations (Dickinson *et al.* 1999; Walker 2002; Sane & Dickinson 2002; Wang *et al.* 2004; Fung 2008).

A major goal has been to formulate mathematical force laws for the various contributing effects during flight and to incorporate these into dynamical models for the free motions of plate-wings (Farren 1935; Sane & Dickinson 2002; Wang *et al.* 2012; Wang 2016). These efforts parallel lift-drag types of laws and flight dynamics models of fixed-wing aircraft (Lee *et al.* 2016; Wang *et al.* 2012). Given the intrinsic unsteadiness in the motions, flows, and forces during passive flight, the suitability of such a framework for the falling plate problem is not clear a priori. However, there have been notable successes with quasi-steady aerodynamic models that express forces in terms of instantaneous kinematic state variables, i.e. the plate's orientation or attack angle, translational and rotational velocities, etc. (Andersen *et al.* 2005*a*; Pesavento 2006; Wang *et al.* 2012; Hu & Wang 2014; Nakata *et al.* 2015). Recent work by Li *et al.* (2022) represents the current state of the art for models of the two-dimensional (2D) problem pertaining to planar motions of a thin plate, a setting that is recognized as involving much of the essential physics (Andersen *et al.* 2005*b*; Wang *et al.* 2016; Wang 2016). This nonlinear model built on and extended previous work to account for lift, drag, and added-mass effects associated with translation and rotation, as well as the torques associated with a dynamic center of pressure. The latter was shown to be important to account for the rich variety of motions displayed by plates of differing centers of mass, including end-over-end tumbling, back-and-forth fluttering, phugoid-like bounding, gliding and downward diving. Such states manifest differently in experiments with plastic plates falling in water and paper sheets in air, and the model was shown to successfully account for observations across these systems (Li *et al.* 2022).

As more observations become explainable by flight models, and more aerodynamic effects and conditions are subsumed within a single framework, new questions arise and new research directions become available. These include aspects of how the many different physical parameters defining the plate-fluid system map to the passive-flight states. Models are particularly well suited to address such issues given their efficiency, computational ease compared to direct numerical simulations, and versatility compared to experiments (Sane & Dickinson 2002; Dickson & Dickinson 2004; Andersen *et al.* 2005*b*; Wang 2016). Further, exploration of a given model's solution space should furnish new predictions that can be tested against other methods and therefore establish its applicability in different parameter regimes or drive its further refinement. Such work is motivated by the many potential applications. Quasi-steady modeling has already proven highly effective for insect flight (Birch & Dickinson 2003; Liu 2005; Bergou *et al.* 2010; Ristroph *et al.* 2010, 2011, 2013), and other forms of motion and locomotion through air and water such as plant seed dispersal or finned propulsion may similarly benefit (Liu 2005; Miller *et al.* 2012; Wang *et al.* 2018; Certini 2023). For engineered systems such as small-scale flying and swimming vehicles and robots, accurate models could accelerate the design process and integrate into actuation and

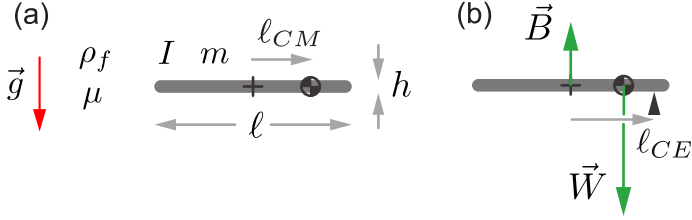


Figure 1: Quantities relevant to the passive flight of a thin plate. (a) A plate of length  $\ell$  and thickness  $h$  has mass  $m$ , center of mass  $\ell_{CM}$  measured from the middle, and moment of inertia  $I$ . It moves under the action of gravity (acceleration  $\vec{g}$ ) through an ambient fluid of density  $\rho_f$  and viscosity  $\mu$ . (b) The center of static equilibrium  $\ell_{CE}$  is defined as the balance point for the torques due to weight and buoyancy.

control schemes (Ellington 1999; Keennon *et al.* 2012; Ristroph & Childress 2014; Jafferis *et al.* 2019).

In this work, we build on the model of Li *et al.* (2022) to undertake an exploration of the space of passive-flight patterns across the widely ranging scales and conditions commonly accessed in aerial and aquatic environments. Dimensional analysis allows us to reduce the complexity of the parameter space for plates of various physical characteristics moving through fluids of differing material properties, and stability analysis of equilibrium solutions to the model yields maps that help to predict and characterize the flight behaviors. These investigations show that the full gamut of flight motions arise across the space of parameters, and that any given state such as gliding can be achieved in distinct ways. This work also spurs useful refinements of the model, furnishes formulas for the stability of steady motions, and leads to the discovery of new unsteady motions. Overall, these results reveal an unexpectedly complex space of passive-flight behaviors that can, however, be organized and understood through the presented modeling and analysis techniques.

## 2. Dimensional and scaling analyses

We seek to establish dimensionless groups of variables with which to describe the general problem of a rigid plate of arbitrary mass distribution that passively falls under gravity through a Newtonian fluid. We follow previous works and address the two-dimensional problem (Andersen *et al.* 2005a; Li *et al.* 2022; Sane & Dickinson 2002; Hu & Wang 2014). The situation is characterized by the 8 dimensional quantities shown in figure 1a. There are 5 quantities intrinsic to the plate: chord length,  $\ell$ ; thickness,  $h$ ; center of mass,  $\ell_{CM}$ ; the 2D mass,  $m$ , as measured per unit span; and 2D moment of inertia,  $I$ . There are 3 additional environmental quantities: fluid density,  $\rho_f$ ; dynamic viscosity,  $\mu$ ; and the gravitational acceleration,  $\vec{g}$ . These 8 total quantities may be reduced by the Buckingham  $\pi$  theorem to 5 dimensionless groups (Logan 2013). Reasonable choices consistent with the aerodynamics literature are (Andersen *et al.* 2005a; Li *et al.* 2022):

$$\ell_{CM}^* = \frac{\ell_{CM}}{\ell}, \quad h^* = \frac{h}{\ell}, \quad M^* = \frac{m}{\pi \rho_f \left(\frac{\ell}{2}\right)^2}, \quad I^* = \frac{I}{\frac{1}{2} \pi \rho_f \left(\frac{\ell}{2}\right)^4}, \quad Re = \frac{\sqrt{2mg\rho_f\ell}}{\mu}. \quad (2.1)$$

Respectively, these correspond to the normalized center of mass, the thickness aspect ratio, the mass of the plate relative to the fluid, the relative moment of inertia, and the Reynolds number  $Re = \rho_f U \ell / \mu$  based on a speed scale  $U = \sqrt{2mg/\rho_f\ell}$  set by balancing weight with a fluid force of the usual high- $Re$  form that increases quadratically with speed.

Anticipating applications for different fluids, we consider a related set of parameters

Quantity	Definition	Range
Center of equilibrium, $\ell_{CE}^*$	$\frac{\ell_{CM}^*}{W^*}$	$[0, \infty)$
Effective weight, $W^*$	$1 - \frac{\rho_f h \ell}{m}$	$(0, 1)$
Mass, $M^*$	$\frac{m}{\pi \rho_f (\ell/2)^2}$	$(0, \infty)$
Moment of inertia, $I^*$	$\frac{2I}{\pi \rho_f (\ell/2)^4}$	$(0, \infty)$
Reynolds number, $Re$	$\frac{\sqrt{2W^* m g \rho_f \ell}}{\mu}$	$(10^2, 10^5)$

Table 1: Summary of dimensionless quantities and their ranges for the problem of a thin plate falling passively under gravity through fluid.

that explicitly includes the effect of buoyancy. To this end, it is convenient to define the dimensionless form of the buoyancy-corrected weight  $W^* = (W - B)/W = 1 - \rho_f h \ell / m = 1 - 4h^*/\pi M^*$ . The last two expressions hold specifically for a plate of rectangular cross-section, and the final form indicates that  $W^*$  may replace  $h^*$  in the dimensionless set of variables. Further, the Reynolds number is readily modified by replacing the weight with its buoyancy-corrected form:  $mg \rightarrow W^*mg$  (Amin *et al.* 2019). We also replace the center of mass with the more general center of static equilibrium, which is the location at which the torques due to buoyancy and weight balance in a static situation without flow (Li *et al.* 2022). Torque balance based on the force diagram of figure 1b leads to the relation  $\ell_{CE} = \ell_{CM}/W^*$ . In summary, the selected 5 dimensionless groups can be expressed in terms of the 8 dimensional plate-fluid quantities as:

$$\ell_{CE}^* = \frac{\ell_{CM}}{W^* \ell}, \quad W^* = 1 - \frac{\rho_f h \ell}{m}, \quad M^* = \frac{m}{\pi \rho_f \left(\frac{\ell}{2}\right)^2}, \quad I^* = \frac{I}{\frac{1}{2} \pi \rho_f \left(\frac{\ell}{2}\right)^4}, \quad Re = \frac{\sqrt{2W^* m g \rho_f \ell}}{\mu}. \quad (2.2)$$

These parameter definitions are summarized in table 1 along with their ranges.

The variables  $\ell_{CE}^*$ ,  $W^*$ ,  $M^*$ , and  $I^*$  will appear throughout our study, and we will examine their effect within a model. The parameter  $Re$  will not appear explicitly but is implicitly assumed to be intermediate (between  $10^2$  and  $10^5$ ) to reflect the range over which we expect the model to be applicable. The model and our results will, strictly speaking, pertain to thin plates of rectangular cross-section in accordance with the expressions in equation 2.2. However, the form of the model may be more generally relevant to slender wings whose shape would dictate the aerodynamic force coefficients (e.g. lift, drag, and added mass) that appear in the model. One may also reasonably apply our results to flight systems composed of a thin wing as the aerodynamically relevant surface and other structures that experience significantly weaker fluid forces but nonetheless contribute (perhaps strongly) to mass, buoyancy, center of mass, moment of inertia, etc. For example, a gliding bird could be crudely viewed in this way as composed of wings and a body (fuselage).

### 2.1. Survey of intermediate- $Re$ passive fliers

The need for a general analysis of the passive flight problem is motivated by the widely ranging parameter values characterizing the relevant systems. In figure 2 we place some representative fliers on the 3D map defined by the quantities  $(W^*, M^*, I^*)$ , whose values can be estimated from information in the literature (Appendix A). Reliable data is less available for  $\ell_{CE}^*$ , whose values presumably span 0 for symmetric bodies to order one for those unevenly

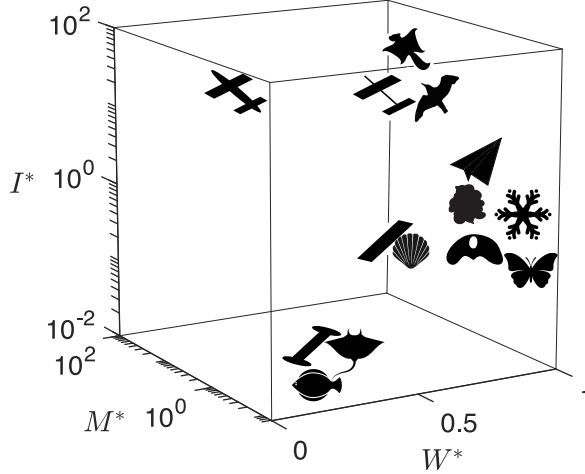


Figure 2: Real-world flight systems occupy different regions of the parameter space. The selected examples vary in size and composition and occupy either air or water, and they rely on thin structures operating at intermediate Reynolds numbers. Proceeding roughly from top to bottom, shown are a flying squirrel, an autonomous gliding water craft, a gliding air vehicle, a bird, a paper airplane, a particulate of marine snow, a snowflake, an aluminum plate in water, a scallop, a seed, a butterfly, an acrylic plate in water, a stingray in water, and a flounder.

weighted. The examples displayed include laboratory idealizations involving metal or plastic plates in water; the everyday case of paper in air; flying animals such as insects, mammals and birds; swimming animals such as mollusks, fish and rays; plant seeds; biomimetic robots; and abiotic fliers such as marine snow and airborne snowflakes. What these have in common is that all have thin structures that dictate their intermediate- $Re$  motions through fluids.

Some further details give greater appreciation for the diversity among the relevant systems. Proceeding generally top to bottom, shown in figure 2 are a flying squirrel (*Glaucomys volans*) (Thorington Jr & Heaney 1981), an autonomous gliding water vehicle (Wood & Inzartsev 2009), an autonomous gliding air vehicle (Wood *et al.* 2007), a bird (*Uria aalge*) (Berg & Rayner 1995), a paper airplane (Li *et al.* 2022), a flake of marine snow (Passow *et al.* 2012), a snowflake (Langleben 1954), an aluminum plate in water (Andersen *et al.* 2005b), a scallop (*Placopecten magellanicus*) (Cheng *et al.* 1996), a seed (*Alsomitra macrocarpa*) (Viola & Nakayama 2022; Ennos 1989), a butterfly (*Papilio ulysses*) (Hu & Wang 2010), a plastic plate in water (Li *et al.* 2022), a stingray in water (*Dasyatis pastinaca*) (Yigin & Ismen 2012), and a flounder (*Paralichthys olivaceus*) (Takagi *et al.* 2010). As detailed in the Appendix, the parameters ( $W^*$ ,  $M^*$ ,  $I^*$ ) are computed as order-of-magnitude estimates based on reported values of the relevant morphological parameters and dimensions.

Can a single model usefully apply across such large variations in parameter values? Are steady motions such as gliding only available in restricted regions of the space, or are they generally accessible? How does the stability of such states vary with the parameters? These are some of the questions motivating the work presented here.

### 3. Existence and uniqueness of free-flight equilibrium states

Our characterizations start by seeking to identify the equilibrium flight states that satisfy zero net force and torque and which therefore involve steady translation and rotation. Such motions are specified by the constant values of 3 kinematic variables, which would generally be the

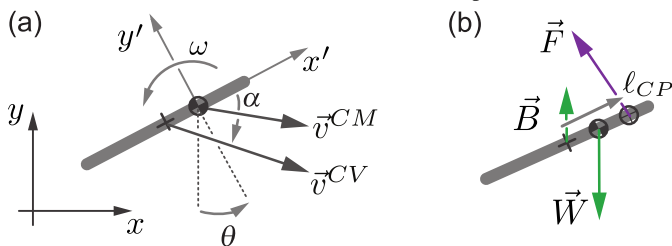


Figure 3: Definitions of dynamic quantities. (a) A snapshot of the plate. The center of mass has location  $(x, y)$  in the lab frame and translates with velocity  $\vec{v}^{CM}$ , and the plate has posture given by the angle  $\theta$  and rotates with angular velocity  $\omega$ . The primed frame co-rotates with the plate, and the angle of attack  $\alpha$  is that of the center of volume velocity  $\vec{v}^{CV}$  relative to the  $x'$  axis. (b) Free body diagram of the forces. The net aerodynamic force  $\vec{F}$  acts at the center of pressure  $\ell_{CP}$ , the weight  $\vec{W}$  acts at the center of mass, and the buoyancy  $\vec{B}$  acts at the center of volume (middle).

rotation rate  $\omega$  and the two components of the center of mass velocity  $\vec{v}^{CM} = (v_x^{CM}, v_y^{CM})$ . These and other free-flight variables are defined in figure 3a. However, rotation can be immediately excluded on the basis that such states generally involve time-dependent fluid forces and torques. It is therefore the special cases with  $\omega = 0$  that are of interest, for which we instead choose the orientation angle  $\theta$  defined relative to the vertical and the velocity  $\vec{v}$ , which is the same for any point on the wing. Equivalently, the state is specified by  $\theta$ , the speed  $v = |\vec{v}|$ , and angle of attack  $\alpha$  from the plate surface to its velocity vector. These 3 kinematic constants combine with the many dimensional parameters (8 for rectangular plates) characterizing the wing-fluid system by a grand total of 11 quantities which specify the wing-fluid-flight system. However, these quantities are not independent, and a subset may determine the others.

Here we claim a correspondence principle: *specifying the static quantities that arise for a wing fixed in a wind tunnel setting determines the full set of dynamical quantities involved in its free-flight equilibrium at the same relative flow conditions.* That is, for a wing of given geometry (shape and size) fixed in a given fluid (density and viscosity) under steady flow conditions (attack angle and speed), one can determine the remaining factors (orientation and trajectory of the wing, its mass, center of mass, and moment of inertia) needed to achieve the same aerodynamic conditions as an equilibrium motion through the fluid under gravity. We believe the claim is applicable generally to wings in the sense of thin structures at moderate to high  $Re$ . The equilibria may or may not be aerodynamically stable.

The argument starts in the wind tunnel setting, where a wing is held fixed in a steady uniform flow of speed  $v$  at angle of attack  $\alpha'$ , defined as that of the plate relative to the flow as shown in figure 4a. These factors determine the aerodynamic force  $\vec{F}$  due to pressure and the center of pressure  $\ell_{CP}$ , which is the effective point of action. The entire wing-tunnel system can be rotated to make  $\vec{F}$  point vertically upward as in figure 4b. This determines the plate orientation angle  $\theta$  while keeping  $\alpha'$  and  $v$  at their prescribed values. The wing may then be released from rest within this inclined flow. Force balance is achieved only if the fluid force balances the buoyancy-corrected weight,  $F = W - B$ , which therefore determines the mass  $m$  since the buoyancy is fixed by the prescribed geometry. Torque balance is achieved only by matching the pressure and equilibrium centers,  $\ell_{CP} = \ell_{CE}$ , which determines the center of mass  $\ell_{CM}$ . The wing may now hover in place within the inclined flow. Invoking Galilean relativity as in figure 4c, the same aerodynamic conditions are realized in free flight through a quiescent fluid by a downward trajectory of the wing at speed  $v^{CV} = v$  and  $\alpha = -\alpha'$ , defined here as that of the velocity vector relative to the plate. The moment

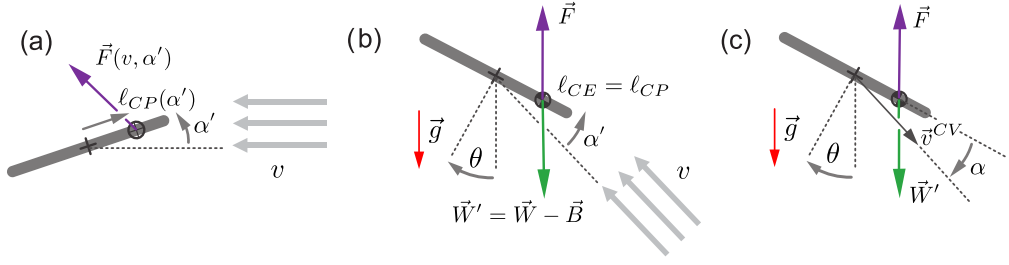


Figure 4: The aerodynamic conditions of a fixed wing in a wind tunnel flow can be identically realized as an equilibrium state of free flight. (a) A plate held fixed at attack angle  $\alpha' > 0$  in a wind tunnel of flow speed  $v$  experiences an aerodynamic force  $\vec{F}(v, \alpha')$  that acts at the center of pressure  $l_{CP}(\alpha')$ . (b) The entire plate-tunnel system can be rotated so that  $\vec{F}$  points directly upward, which determines the orientation angle  $\theta$ . The plate can then be released under gravity, and its total mass may be assigned such that  $|\vec{W}'| = |\vec{F}|$  in order to achieve force balance. The mass may be distributed such that  $l_{CE} = l_{CP}$ , which ensures torque balance. (c) A change of reference frames indicates that the same conditions can be achieved as an equilibrium motion through quiescent fluid. Note the wind-tunnel convention defines the attack angle  $\alpha'$  as that of the plate relative to the upstream direction, whereas the free-flight angle  $\alpha = -\alpha'$  is defined here as that of the plate velocity vector relative to the  $x'$  axis.

of inertia  $I$  is undetermined but irrelevant, i.e. any identified equilibrium may be achieved for any value of  $I > 0$ . This specifies the sense in which free-flight equilibria exist and are unique.

Note that  $\alpha' = 0$  is a special case in that there is no torque,  $l_{CP}$  is undefined, and  $l_{CE}$  is thus undetermined. While any location of the center of mass is permissible, the other free-flight factors such as mass, velocity, and attack angle are determined according to the reasoning given above.

In summary, this argument takes as inputs the wing geometry (for a plate,  $\ell$  and  $h$ ), the fluid and environmental parameters ( $\rho_f$ ,  $\mu$  and  $g$ ), and the usual wind tunnel quantities ( $\alpha'$  and  $v$ ) and from these determines the remaining quantities ( $\theta$ ,  $m$  and  $l_{CM}$ , with  $I$  free) needed to completely specify a free-flight equilibrium state. This argument is not unique, e.g. one could take the plate mass  $m$  and free-flight attack angle  $\alpha$  as inputs to determine the speed  $v$ . Parallel reasoning within the dimensionless variables using this modified argument takes as inputs ( $\alpha$ ,  $W^*$ ) to determine ( $\theta$ ,  $\vec{v}^{CV*}$ ,  $l_{CE}^*$ ) with  $I^*$  and  $M^*$  being free. We will exploit this result in the coming analyses of equilibria and their stability.

Implicit in the above argument are conditions that are often assumed in aerodynamic contexts and which will be exactly satisfied within our quasi-steady framework. The fluid force and torque must derive dominantly from pressure, as expected for sufficiently high  $Re > 10^2$  (Tritton 2012). The forces are assumed steady, as expected for low  $\alpha$  and stably attached boundary layer flows at sufficiently low  $Re < 10^5$  (Schlichting & Gersten 2016; Anderson 2011). (Alternatively, one may consider the force balances defining the equilibria as applying in the time average.) Slenderness of the wing is needed so that the center of pressure is well defined via integrals along the centerline of the pressure difference across the surface:  $l_{CP} = \int xp(x)dx / \int p(x)dx$ . For a given wing geometry, the pressure center  $l_{CP}(\alpha')$  is assumed to depend only on the attack angle. Finally, for a given wing at fixed  $\alpha'$  in a given directed flow, the fluid force  $\vec{F}$  is assumed to have a unique direction, and its magnitude has a one-to-one (bijective) relationship with the relative flow speed. Such conditions are expected insofar as the flow state is unique for a given set of conditions and



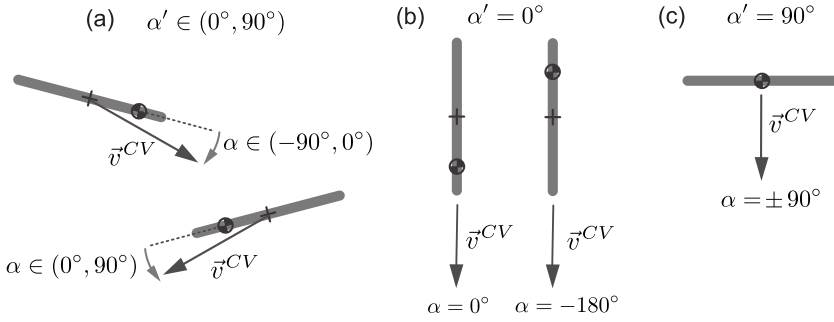


Figure 5: Three types of free-flight equilibria of a plate. (a) Gliding involves constant speed motion along a sloped trajectory and with an acute angle of the plate. Each attack angle  $\alpha' \in (0, \pi/2) = (0^\circ, 90^\circ)$  as conventionally defined for the wind tunnel setting admits two free-flight states with  $\alpha = \pm\alpha'$  corresponding to leftward and rightward gliding. (b) Diving involves constant speed descent directly downward and with edgewise posture of the plate. For a given value of  $\ell_{CE}^* \geq 0$ , two such states exist. (c) Pancaking involves constant speed descent directly downward and with broadside-on posture. This is achieved only for  $\ell_{CE}^* = 0$ , and thus the two states are physically identical and degenerate.

for pressure forces that typically increase quadratically with speed at moderate to high  $Re$  (Tritton 2012; Anderson 2011).

### 3.1. Equilibrium states for plates

The fixed- and free-flight correspondence principle readily allows all equilibria to be tabulated based on the attack angle, and the possibilities are depicted in figure 5. For this purpose, it is helpful to distinguish two notions of the angle of attack. The static angle  $\alpha' \in [0, \pi/2] = [0^\circ, 90^\circ]$  is relevant to the fixed configuration of a wind tunnel, where the limited range is sufficient for completely specifying the aerodynamic properties of a plate given its fore-aft and up-down symmetries. The dynamic angle  $\alpha \in [-\pi, \pi] = [-180^\circ, 180^\circ]$  is relevant to free-flight, where the full range is needed to completely specify the flight state and allow for all possible directions of the velocity vector relative to the plate's  $x'$ -axis.

We use the term *gliding* for those states with strictly acute static angle  $\alpha' \in (0, \pi/2) = (0^\circ, 90^\circ)$ , as shown in figure 5a. For a given static  $\alpha'$ , there are two available free-flight motions that take the form of leftward and rightward descent along linear trajectories for which the dynamic angles are  $\alpha = \pm\alpha'$ . It will be shown that gliding at a given  $\alpha'$  is associated with a unique value of the equilibrium center  $\ell_{CE}^*$ .

We introduce special terms for the equilibria at the two extremes of  $\alpha'$ . We use the term *diving* for those states with  $\alpha' = 0 = 0^\circ$ , which involve edge-on and strictly downward descent as shown in figure 5b. For a given  $\ell_{CE}^* > 0$ , there are two available free-flight motions that take the form of bottom-heavy diving with  $\alpha = 0 = 0^\circ$  and top-heavy diving with  $\alpha = -\pi = -180^\circ$ . The two are distinguished by whether the center of equilibrium is displaced towards the leading or trailing edge, and they are degenerate for the symmetric case of  $\ell_{CE}^* = 0$ . Diving is exceptional in that torque balance is achieved for all values of  $\ell_{CE}^* \geq 0$ , as the weight and aerodynamic force both act parallel to the plate, and it will necessitate a separate analysis of stability. We use the term *pancaking* for those states with  $\alpha' = \pi/2 = 90^\circ$ , which involve broadside-on and strictly downward descent as shown in figure 5c. These states will be shown to exist only for the symmetric case  $\ell_{CE}^* = 0$ . In principle, they take the form of two motions with  $\alpha = \pm\pi/2 = \pm 90^\circ$ , which however are degenerate and physically indistinguishable. Within our quasi-steady model and its analysis, pancaking is simply a particular case of gliding that requires no special treatment.



#### 4. Flight dynamics model and numerical solutions

We propose and analyze a dynamical system for the problem of a falling plate that builds on and extends the work of Li *et al.* (2022). The model expresses the Newton-Euler equations for planar (2D) motion with forces and torques due to gravity (weight), fluid-static effects (buoyancy) and fluid-dynamic effects (pressure, skin friction, added mass, etc.). As shown in figure 3a, the plate has center-of-mass position  $(x, y)$  in the lab (fixed) frame and center-of-mass velocity  $\vec{v}^{CM} = (v_x^{CM}, v_y^{CM})$ . Its instantaneous orientation angle is  $\theta$  and its angular velocity is  $\omega$ . It proves most convenient to express the dynamical variables in a frame that rotates with the plate, e.g.  $(v_{x'}^{CM}, v_{y'}^{CM})$ , where the prime indicates the co-rotating frame (figure 3a). The aerodynamic forces and torques are expressible in terms of the motion of the geometric middle or center of volume CV,

$$v_{x'}^{CV} = v_{x'}^{CM} = v_{x'} \quad \text{and} \quad v_{y'}^{CV} = v_{y'}^{CM} - \omega \ell_{CM} = v_{y'} - \omega \ell_{CM}, \quad (4.1)$$

where we suppress the superscript CM hereafter for ease of notation. The dynamics take the form of a system of nonlinear, coupled ordinary differential equations (ODEs) whose dimensional form is given by:

$$\begin{aligned} \dot{x} &= v_{x'} \cos \theta - v_{y'} \sin \theta \\ \dot{y} &= v_{x'} \sin \theta + v_{y'} \cos \theta \\ \dot{\theta} &= \omega \\ (m + m_{11})\dot{v}_{x'} &= (m + m_{22})\omega v_{y'} - m_{22}\omega^2 \ell_{CM} + L_{x'} + D_{x'} - m'g \sin \theta \\ (m + m_{22})\dot{v}_{y'} &= -(m + m_{11})\omega v_{x'} + m_{22}\dot{\omega} \ell_{CM} + L_{y'} + D_{y'} - m'g \cos \theta \\ (I + I_a)\dot{\omega} &= \tau_T + \tau_{RL} + \tau_{RD} + \tau_B. \end{aligned} \quad (4.2)$$

This model is identical to that of Li *et al.* (2022) with the exception of the term  $\tau_{RL}$ , which is newly added here and will be discussed below. The first three equations relate positions and angle to their respective velocities, and the last three equations are the Newton-Euler equations for the accelerations induced by forces and torques. Added mass effects are associated with terms involving the coefficients  $m_{11} = 0$ ,  $m_{22} = \pi \rho_f \ell^2 / 4$  and  $I_a = I_a(\ell_{CM} = 0) + m_{22} \ell_{CM}^2 = \pi \rho_f \ell^4 [1 + 8(2\ell_{CM}/\ell)^2] / 128$ , where the expressions hold for an infinitesimally thin plate. The lift  $\vec{L}$  and drag  $\vec{D}$  terms are detailed below and expressed in terms of the velocities and posture of the plate, with force coefficients that were empirically determined by Li *et al.* (2022) for intermediate *Re*. Aerodynamic effects also induce torques that are decomposed into  $\tau_T$ ,  $\tau_{RL}$  and  $\tau_{RD}$  according to their association with lift and drag from wing translation (T), lift from rotation (RL) and drag from rotation (RD). Finally, buoyancy effects are accounted for in the corrected mass  $m' = (\rho_s - \rho_f)V = (\rho_s - \rho_f)h\ell$  for a plate of homogeneous density  $\rho_s$  and 2D volume  $V$ , as well as in the torque  $\tau_B$  about the center of mass. These quantities are defined as follows:

$$\begin{aligned}
\vec{L}_T &= \frac{1}{2} \rho_f \ell C_L(\alpha) \sqrt{v_{x'}^2 + (v_{y'} - \omega \ell_{CM})^2} (v_{y'} - \omega \ell_{CM}, -v_{x'}) \\
\vec{L}_R &= -\frac{1}{2} \rho_f \ell^2 C_R \omega (v_{y'} - \omega \ell_{CM}, -v_{x'}) \\
\vec{L} &= \vec{L}_T + \vec{L}_R \\
\vec{D} &= -\frac{1}{2} \rho_f \ell C_D(\alpha) \sqrt{v_{x'}^2 + (v_{y'} - \omega \ell_{CM})^2} (v_{x'}, v_{y'} - \omega \ell_{CM}) \\
\tau_T &= -\frac{1}{2} \rho_f \ell \sqrt{v_{x'}^2 + (v_{y'} - \omega \ell_{CM})^2} [C_L(\alpha) v_{x'} + C_D(\alpha) (v_{y'} - \omega \ell_{CM})] [\ell_{CP}(\alpha) - \ell_{CM}] \\
\tau_{RL} &= \frac{1}{2} \rho_f \ell C_R \omega v_{x'} (\ell_{CM} - \ell_{CRL}) \\
\tau_{RD} &= -\frac{1}{128} C_D^{\pi/2} \omega |\omega| [(2\ell_{CM}/\ell + 1)^4 + (2\ell_{CM}/\ell - 1)^4] \\
\tau_B &= -\rho_f g h \ell \ell_{CM} \cos \theta.
\end{aligned} \tag{4.3}$$

The various aerodynamic coefficients are largely taken from Li *et al.* (2022), where they were determined by theoretical considerations and experimental measurements. The rotational lift coefficient  $C_R = 1.1$  is a constant, as is the effective point of action or center of rotational lift  $\ell_{CRL} = 0$ . Other quantities depend on the dynamic attack angle  $\alpha = \arctan[(v_{y'} - \ell_{CM}\omega)/v_{x'}]$ , including the lift coefficient  $C_L(\alpha)$ , drag coefficient  $C_D(\alpha)$  and center of pressure  $\ell_{CP}(\alpha)$ . The following expressions from Li *et al.* (2022) are appropriate for plates at intermediate  $Re$  and angles  $\alpha \in [0, \pi/2] = [0^\circ, 90^\circ]$ :

$$\begin{aligned}
C_L(\alpha) &= f(\alpha) C_L^1 \sin \alpha + [1 - f(\alpha)] C_L^2 \sin(2\alpha) \\
C_D(\alpha) &= f(\alpha) (C_D^0 + C_D^1 \sin^2 \alpha) + [1 - f(\alpha)] C_D^{\pi/2} \sin^2 \alpha \\
\ell_{CP}(\alpha)/\ell &= f(\alpha) (C_{CP}^0 - C_{CP}^1 \alpha^2) + [1 - f(\alpha)] C_{CP}^2 [1 - \alpha/(\pi/2)] \\
f(\alpha) &= [1 - \tanh(\alpha - \alpha_0)/\delta]/2.
\end{aligned} \tag{4.4}$$

Here, the constant prefactors are  $C_L^1 = 5.2$ ,  $C_L^2 = 0.95$ ,  $C_D^0 = 0.1$ ,  $C_D^1 = 5.0$ ,  $C_D^{\pi/2} = 1.9$ ,  $C_{CP}^0 = 0.3$ ,  $C_{CP}^1 = 3.5$ ,  $C_{CP}^2 = 0.2$ ,  $\alpha_0 = 14^\circ$  and  $\delta = 6^\circ$ . The logistic function  $f(\alpha)$  plays the mathematical role of an indicator function that smoothly transitions between different expressions appropriate for low  $\alpha < \alpha_0$  where the flow over the plate is expected to be stably attached and higher  $\alpha > \alpha_0$  where the flow separates and stall occurs. Figure 6 shows the corresponding curves identified in wind-tunnel experiments by Li *et al.* (2022). The above expressions are readily extended throughout  $\alpha \in [-\pi, \pi] = [-180^\circ, 180^\circ]$  based on symmetries as explained in Li *et al.* (2022), which allows the model to address arbitrary motions during free-flight.

#### 4.1. Torque from rotational lift

We give extra consideration to the torque from rotational lift  $\tau_{RL}$  as it is the only new addition to the model presented in Li *et al.* (2022). That work included rotational lift  $\vec{L}_R$  as a Magnus-like force that is associated with the combined translation and rotation of a wing and which scales with the product of the two respective speeds (Munk 1925; Kramer 1932; Sane 2003). However, no associated torque was included, and indeed to our knowledge no previous work has addressed a possible torque contribution from this effect. Its omission in the model of Li *et al.* (2022) is conceptually problematic, since the absence of an associated

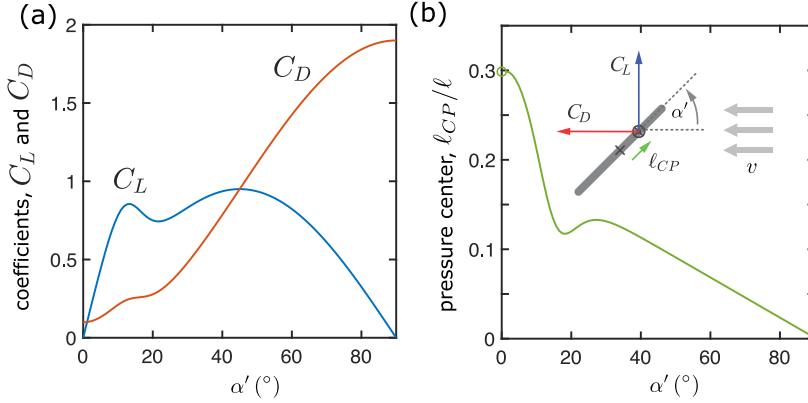


Figure 6: Aerodynamic force characteristics of a thin plate at intermediate  $Re$  as determined by the experimental tunnel measurements of Li *et al.* (2022). (a) Lift and drag coefficients as functions of the attack angle  $\alpha' \in [0, \pi/2] = [0^\circ, 90^\circ]$ , whose range covers all unique postures relative to the flow. Stall is evident in the drop in lift near  $\alpha' = 15^\circ$ . (b) The center of pressure location along the plate. Stall leads to a non-monotonic form of the curve. The value at  $\alpha = 0$  is undefined as the force is parallel to the plate surface.

torque implies that this force always acts at the center of mass. This violates the fundamental physical principle that all fluid dynamical effects depend only on the outer shape and motion of a structure and do not directly “know” about aspects of mass and its distribution inside the structure.

We propose a remedy in which the rotational lift force  $\vec{L}_R$  is associated with an effective point of action or center  $l_{CRL}$ . This is analogous to how pure translation gives rise to pressure forces (translational lift and drag) that act at the center of pressure. As such, the expression for  $\tau_{RL} = L_{R,v}(\ell_{CM} - l_{CRL})$  in equation 4.3 follows directly from that for  $\vec{L}_R$ . The center of rotational lift  $l_{CRL}$  could in principle vary with attack angle and perhaps other dynamical quantities, but such information seems unavailable in the literature. To avoid introducing any unsubstantiated dependencies, we opt for the simplest choice of  $l_{CRL} = 0$ , i.e. the rotational lift always acts at the middle of the plate. This choice could be viewed as consistent with previous models of Andersen *et al.* (2005a,b) that included rotational lift without any associated torque for symmetrically weighted plates, which have  $l_{CM} = 0$  and hence  $\tau_{RL} = 0$  only if  $l_{CRL} = 0$ . Future experiments or numerical simulations may provide more information about this effect, and the model may be updated accordingly.

#### 4.2. Dimensionless form of dynamical system

Nondimensionalization of the ODE system leads to equivalent expressions that involve the aforementioned dimensionless variables ( $l_{CE}^*$ ,  $W^*$ ,  $M^*$ ,  $I^*$ ,  $Re$ ). We choose the characteristic length scale to be  $\ell$  and time scale to be  $\ell/U$ , recalling the characteristic speed  $U =$

$\sqrt{2W^*mg/\rho_f\ell}$ . The dynamical system then becomes

$$\begin{aligned}\dot{x}^* &= v_{x'}^* \cos \theta - v_{y'}^* \sin \theta \\ \dot{y}^* &= v_{x'}^* \sin \theta + v_{y'}^* \cos \theta \\ \dot{\theta} &= \omega^*\end{aligned}$$

$$M^* v_{x'}^* = (1 + M^*) \omega^* v_{y'}^* - (\omega^*)^2 W^* \ell_{CE}^* + L_{x'}^* + D_{x'}^* - \frac{2}{\pi} \sin \theta \quad (4.5)$$

$$(1 + M^*) v_{y'}^* = -M^* \omega^* v_{x'}^* + \omega^* W^* \ell_{CE}^* + L_{y'}^* + D_{y'}^* - \frac{2}{\pi} \cos \theta$$

$$\left[ I^* + \frac{1 + 32(W^* \ell_{CE}^*)^2}{4} \right] \dot{\omega}^* = \tau_T^* + \tau_{RL}^* + \tau_{RD}^* + \tau_B^*.$$

The Reynolds number  $Re$  is the only dimensionless variable that does not appear explicitly, and it should be viewed as implicit in the coefficients of the aerodynamic terms:

$$\begin{aligned}\vec{L}_T^* &= \frac{2}{\pi} C_L(\alpha) \sqrt{(v_{x'}^*)^2 + (v_{y'}^* - \omega^* \ell_{CM}^*)^2} (v_{y'}^* - \omega^* \ell_{CM}^*, -v_{x'}^*) \\ \vec{L}_R^* &= -\frac{2}{\pi} C_R \omega^* (v_{y'}^* - \omega^* \ell_{CM}^*, -v_{x'}^*) \\ \vec{L}^* &= \vec{L}_T^* + \vec{L}_R^* \\ \vec{D}^* &= -\frac{2}{\pi} C_D(\alpha) \sqrt{(v_{x'}^*)^2 + (v_{y'}^* - \omega^* \ell_{CM}^*)^2} (v_{x'}^*, v_{y'}^* - \omega^* \ell_{CM}^*) \\ \tau_T^* &= -\frac{16}{\pi} \sqrt{(v_{x'}^*)^2 + (v_{y'}^* - \omega^* \ell_{CM}^*)^2} \left[ C_L(\alpha) v_{x'}^* + C_D(\alpha) (v_{y'}^* - \omega^* \ell_{CM}^*) \right] [\ell_{CP}^*(\alpha) - \ell_{CM}^*] \\ \tau_{RL}^* &= -\frac{16}{\pi} C_R \omega^* v_{x'}^* (\ell_{CM}^* - \ell_{CRL}^*) \\ \tau_{RD}^* &= -\frac{1}{4\pi} C_D^{\pi/2} \omega^* |\omega^*| \left[ (2\ell_{CM}^* + 1)^4 + (2\ell_{CM}^* - 1)^4 \right] \\ \tau_B^* &= -\frac{16}{\pi} (1 - W^*) \ell_{CE}^* \cos \theta.\end{aligned} \quad (4.6)$$

Here  $\ell_{CP}^* = \ell_{CP}/\ell$  and  $\ell_{CM}^* = \ell_{CM}/\ell = W^* \ell_{CE}^*$ , and thus only the dimensionless variables  $(\ell_{CE}^*, W^*, M^*, I^*)$  appear explicitly as parameters in the system. The major goals of this work are to understand how the equilibrium solutions and their stability depend on these quantities.

### 4.3. Survey of numerical solutions to the model

To give a sense of the types of motions produced by the model, we present in figure 7 a variety of flight trajectories that arise as numerical solutions of the dynamical system for different parameter values. We hereafter work with the dimensionless system of equations 4.5 and 4.6 and drop the asterisks on  $(\ell_{CE}, W, M, I)$ . These parameters serve as inputs to a ‘‘flight simulator’’ code that numerically integrates the ODEs in Matlab via the built-in solver *ode15s*. The survey shown in figure 7 explores the parameters  $(\ell_{CE}, W, M)$  for fixed  $I = 0.1$ , which is representative in that other values of  $I$  produce similarly diverse sets of motions. Each case is marked by a point in parameter space, and the corresponding numerical solutions are displayed as snapshots of the plate orientation and location over time. All are

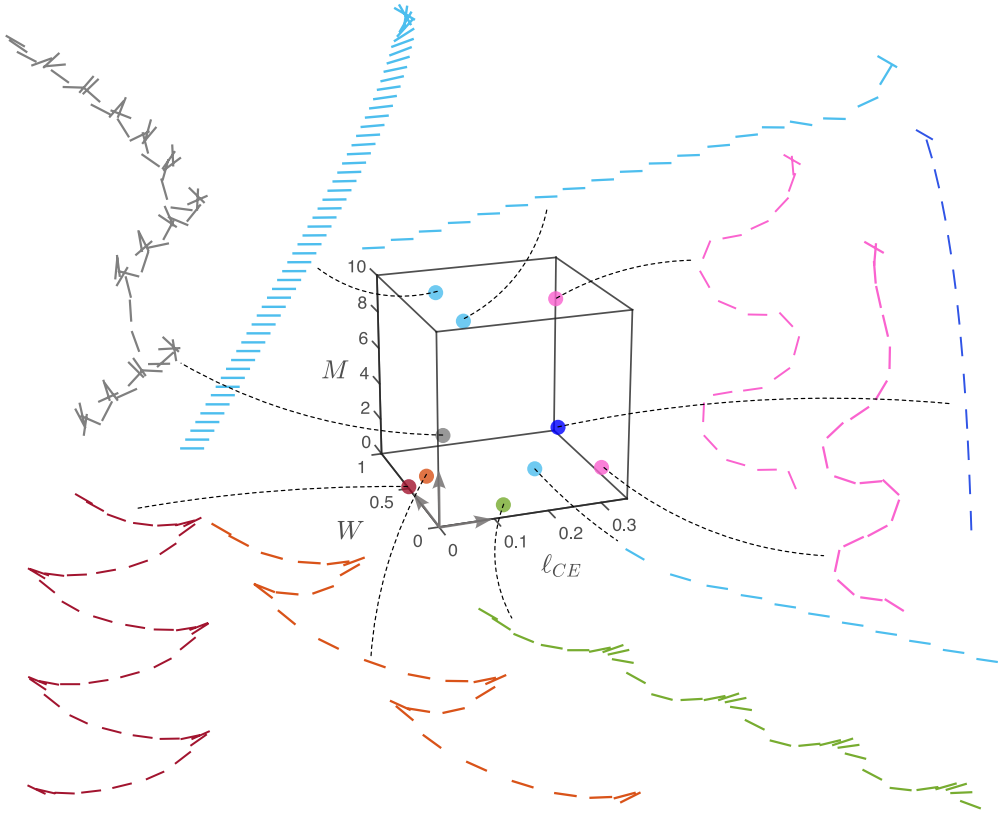


Figure 7: Sample trajectories produced by the flight dynamics model reveal a variety of behaviors. Different values of the parameters ( $l_{CE}$ ,  $W$ ,  $M$ ) for fixed  $I = 0.1$  are marked on the 3D flight map, and the displayed plate motions result from identical initial conditions. Steady terminal states include gliding (light blue) at different attack angles and diving (dark blue) but pancaking is never observed. Periodic states include fluttering (red), progressive fluttering (orange), bounding (green) and meandering (pink). Aperiodic and apparently chaotic motions (grey) with bouts of tumbling are also observed.

released with the same initial conditions, and the resulting terminal or long-time motions vary greatly depending on the inputs.

These samplings of the solution space may be familiar from fluttering leaves, erratically tumbling confetti, and flying paper planes. Some cases lead to steady motions such as sideways gliding (light blue) or downward diving (dark blue). Other cases lead to periodic behaviors such as back-and-forth fluttering with swoops punctuated by sharp reversals (red, orange), phugoid-like bounding with swoops of a single direction (green), or downward meandering along a smoothly winding course (pink). Others seem chaotic with bouts of end-over-end tumbling but lacking any repeated pattern (grey). The same flight pattern may be achieved for significantly different parameter values, and conversely a small change in parameters may lead to substantially different motions.

These explorations make clear the great complexity of the flight space encompassing how the governing parameters map to the eventual dynamical behavior. Importantly, a major result of this work is that one or more of the steady motions (gliding, pancaking and diving) exist as equilibrium solutions at any given point in parameter space. That such states emerge as solutions to the nonlinear model in some regions of parameter space and not others motivates the forthcoming stability analysis. More generally, the identification of equilibrium states and

assessment of their stability will provide a way to systematically characterize the structure and organization of the flight space.

## 5. Analytical forms of the free-flight equilibria

The dynamical flight model admits analytical expressions for the equilibrium states. Here we continue working with the dimensionless system of equations 4.5 and 4.6 without the asterisks on the dimensionless parameters ( $\ell_{CE}$ ,  $W$ ,  $M$ ,  $I$ ). Recalling the reasoning of section 3, equilibria must have  $v_{x'} = v_{y'} = \omega = 0$  and so the nontrivial relations in equation 4.5 reduce to:

$$\begin{aligned} 0 &= L_{x'} + D_{x'} - (2/\pi) \sin \theta \\ 0 &= L_{y'} + D_{y'} - (2/\pi) \cos \theta \\ 0 &= \tau_T + \tau_B. \end{aligned} \quad (5.1)$$

It is immediately clear that neither  $M$  nor  $I$  determine the equilibria, which proves the claim in section 3. That is, if an equilibrium is identified, it may be achieved for any value of either parameter. In contrast,  $\ell_{CE}$  and  $W$  appear in the  $\tau_B$  term per equation 4.6. Expanding the above equations via the definitions in equations 4.6 yields:

$$\begin{aligned} \sqrt{v_{x'}^2 + v_{y'}^2} [C_L(\alpha)v_{y'} - C_D(\alpha)v_{x'}] &= \sin \theta \\ -\sqrt{v_{x'}^2 + v_{y'}^2} [C_L(\alpha)v_{x'} + C_D(\alpha)v_{y'}] &= \cos \theta \\ \sqrt{v_{x'}^2 + v_{y'}^2} [C_L(\alpha)v_{x'} + C_D(\alpha)v_{y'}] [\ell_{CP}(\alpha) - W\ell_{CE}] &= (W - 1)\ell_{CE} \cos \theta. \end{aligned} \quad (5.2)$$

In what follows, we simplify the notation by suppressing the functional dependencies on  $\alpha$  for  $C_L$ ,  $C_D$  and  $\ell_{CP}$ . One can show by manipulating equations 5.2 and invoking the four-quadrant inverse tangent definition of the dynamic attack angle  $\alpha$  that solutions exist for the subset of values  $\alpha \in [-90^\circ, 90^\circ] \cup \{-180^\circ\}$ , these corresponding to downward trajectories. Equivalently, steady-state solutions exist only for static attack angles  $\alpha' \in [0^\circ, 90^\circ]$ . The general solution to all equilibria has the form:

$$(v_{x'}, v_{y'}, \cos \theta, \ell_{CE}) = \left( \frac{\cos \alpha}{(C_L^2 + C_D^2)^{1/4}}, \frac{\sin \alpha}{(C_L^2 + C_D^2)^{1/4}}, -\frac{C_L \cos \alpha + C_D \sin \alpha}{\sqrt{C_L^2 + C_D^2}}, \ell_{CP} \right). \quad (5.3)$$

In the fixed lab frame, this corresponds to motion at constant speed  $v$  along a straight trajectory of angle  $\gamma$  relative to the horizontal:

$$v = \frac{1}{(C_L^2 + C_D^2)^{1/4}} \quad \text{and} \quad \gamma = \alpha + \theta. \quad (5.4)$$

Gliding, diving and pancaking are specific instances within the general set of solutions. Gliding states are those solutions with  $\alpha \in (-\pi/2, 0) \cup (0, \pi/2) = (-90^\circ, 0^\circ) \cup (0^\circ, 90^\circ)$ , or equivalently  $\alpha' \in (0, \pi/2) = (0^\circ, 90^\circ)$ . These arise in pairs of leftward and rightward gliding of oppositely signed  $\alpha = \pm\alpha'$  and orientation angles  $\theta$  differing by  $\pi = 180^\circ$ . Diving states are those solutions with  $\alpha = \{0, -\pi\} = \{0^\circ, -180^\circ\}$ , corresponding respectively to bottom- and top-heavy postures, both of which have  $\alpha' = 0$ . Manipulation of equations 5.2 shows

$\ell_{CE}$  to be a free variable rather than one constrained by  $\ell_{CP}$ . The solution pair for diving is:

$$(v_{x'}, v_{y'}, \theta, \ell_{CE}) = \left( \pm \frac{1}{\sqrt{C_D}}, 0, \mp \frac{\pi}{2} = \mp 90^\circ, \ell_{CE} \geq 0 \right). \quad (5.5)$$

Pancaking states are the pair of solutions with  $\alpha = \pm\pi/2 = \pm 90^\circ$  or  $\alpha' = \pi/2 = 90^\circ$ :

$$(v_{x'}, v_{y'}, \theta, \ell_{CE}) = \left( 0, \mp \frac{1}{\sqrt{C_D}}, -\pi = -180^\circ \text{ or } 0 = 0^\circ, 0 \right), \quad (5.6)$$

which are physically indistinguishable and thus degenerate.

In the following stability analyses, it will be sufficient to confine our attention to those states with  $\alpha \in [0, \pi/2] = [0^\circ, 90^\circ]$ . That is, we need not concern ourselves with distinguishing the paired states, since they share the same stability. The exception is top-heavy diving with  $\alpha = -\pi = -180^\circ$ , which however can be dismissed as statically unstable for all parameters.

## 6. Stability of gliding states

With the dynamical system fully defined and its equilibrium solutions identified, we now seek to understand the parameter ranges for which the equilibria are stable. As such, we conduct a linear stability analysis. Due to the mathematical complexity of the model and its many terms, analytical derivations are available but extremely cumbersome and so we instead employ symbolic computational methods. We develop a code base written in MATLAB that (1) computes equilibria of the ODE system equations 4.5, (2) symbolically linearizes the system about a given equilibrium state, and then (3) assesses the corresponding stability using eigenvalue analysis. Here we again work with the dimensionless variables ( $\ell_{CE}, W, M, I$ ), where the asterisks have been dropped for convenience. The analysis presented here will cover gliding and pancaking states, i.e.  $\alpha \in (0, \pi/2] = (0^\circ, 90^\circ]$ , with diving ( $\alpha = 0 = 0^\circ$  or  $\pi = 180^\circ$ ) to be handled separately.

The inputs to the algorithm are the equilibrium angle of attack  $\alpha \in (0, \pi/2] = (0^\circ, 90^\circ]$ , the normalized and buoyancy-corrected weight  $W \in (0, 1)$ , the relative mass  $M > 0$ , and the relative moment of inertia  $I > 0$ . The code first solves for the unique equilibrium state ( $\ell_{CE} = \ell_{CP}(\alpha), \theta, \vec{v} = \vec{v}^{CM} = \vec{v}^{CV}, \omega = 0$ ), which in all cases verify the analytical results of section 5. Then the Taylor expansion toolbox in MATLAB is used to symbolically linearize the dimensionless ODEs 4.5 about this equilibrium. The algorithm then computes the eigenvalues  $\lambda_i$  of this linearized system, of which there are 4 in accordance with the 4 degrees of freedom ( $v_{x'}, v_{y'}, \theta, \omega$ ). Finally, the code assesses the stability of a particular equilibrium state by checking the sign of the real component of each eigenvalue. If the real components of the eigenvalues are all negative, then the equilibrium is classified as *stable*. If there exists at least one eigenvalue with positive real component, then the equilibrium is unstable. Moreover, if any of these eigenvalues with positive real component also has a zero imaginary component, then the unstable equilibrium is called *statically unstable*; otherwise, it is called *dynamically unstable*. In summary, the progression is as follows:

$$(\alpha, W, M, I) \Rightarrow (\ell_{CE}, \theta, \vec{v}) \Rightarrow \lambda_i \Rightarrow \begin{cases} \text{stable} & \forall i, \text{Re}(\lambda_i) < 0 \\ \text{statically unstable} & \exists i \text{ s.t. } \text{Re}(\lambda_i) > 0, \text{Im}(\lambda_i) = 0 \\ \text{dynamically unstable} & \text{otherwise} \end{cases}$$

In summary, the 4-dimensional input space ( $\alpha, W, M, I$ ) is mapped to an output characterization that assumes one of the three possible classifications (stable, statically unstable, dynamically unstable), each of which corresponds to some steady or unsteady flight pattern. Since  $\alpha \in (0, \pi/2] = (0, 90^\circ]$  maps to a unique  $\ell_{CE}$ , we may also consider the analogous



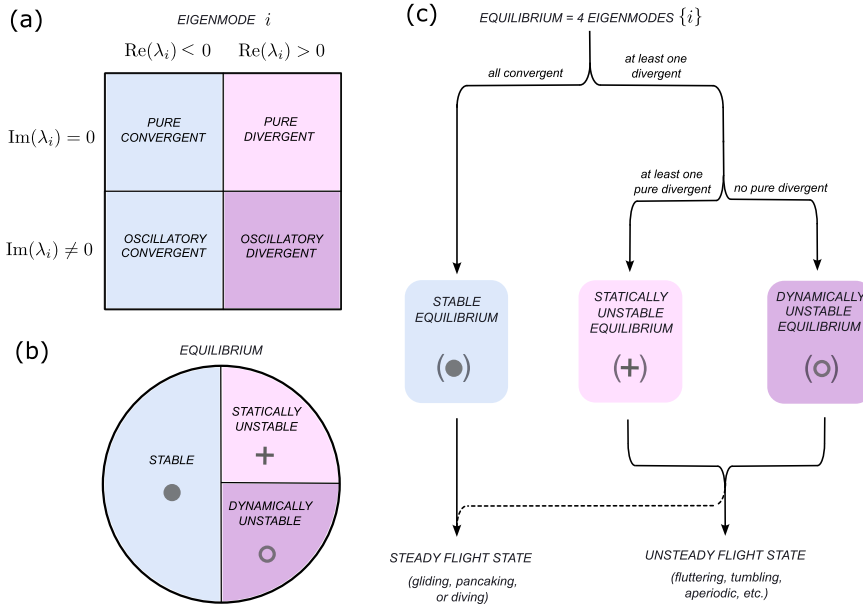


Figure 8: Classification schemes and nomenclature for eigenmodes and free-flight equilibria. (a) Each eigenmode  $i$  may be one of four types based on the real and imaginary parts of its eigenvalue  $\lambda_i$ . (b) Each free-flight equilibrium may be one of three types: stable (blue), statically unstable (pink), or dynamically unstable (purple). (c) Flow diagram showing how the type of equilibrium is determined from the types of eigenmodes. Each equilibrium has 4 eigenmodes, and the presence or absence of certain mode types determines the stability status.

map from  $(\ell_{CE}, W, M, I)$  to (stable, statically unstable, dynamically unstable). This recasts all input parameters as the intrinsic physical properties of the plate-fluid system.

This classification scheme and the associated nomenclature has a specificity and mathematical rigor that may be beyond what is typical in the flight dynamics literature (Etkin & Reid 1995; Anderson & Bowden 2005; Anderson 2011). The schematics of figure 8 relate the various terms. An *equilibrium* is a set of dynamical parameters needed to specify a free-flight motion that balances forces and torques. Each equilibrium has 4 eigenvectors and associated eigenvalues that emerge from a stability analysis, and we call these modes or, more specifically, *eigenmodes*. As shown in panel (a), each eigenmode may be classified as one of 4 types with labels of *convergent* or *divergent* based on its real part and *pure* or *oscillatory* based on its imaginary part. As shown in (b), each equilibrium may be classified as being one of 3 types with names *stable*, *statically unstable*, or *dynamically unstable*. As specified in (c), the presence or absence of certain types of eigenmodes determines the stability status of the equilibrium. Namely, a stable equilibrium has no divergent eigenmodes, a statically unstable equilibrium has at least one pure divergent eigenmode, and a dynamically unstable equilibrium has one or more divergent modes none of which are pure.

These classifications and terms have some relations to free flight. We use the term *free-flight state*, *flight state*, or simply *state* to describe the long-time or terminal behavior exhibited by the dynamical system for a set of parameters specifying an equilibrium. As shown in panel (c), a stable equilibrium will necessarily lead to a *steady state* with the same characteristics (speed, attack angle, etc.) of the equilibrium, and so we call the state by same name of gliding, pancaking or diving used for the equilibrium. An unstable equilibrium of either type will typically lead to an *unsteady state*, including periodic motions such as fluttering or

tumbling and also aperiodic or non-repeating motions. However, the status of an equilibrium as statically or dynamically unstable tells us nothing of the nature of the free flight state beyond that it must be different from the equilibrium. Moreover, as indicated by the dashed route in (c), a given unstable equilibrium may in some cases exhibit a steady state whose dynamical parameters differ from the equilibrium. For example, an unstable diving equilibrium may lead to a stable gliding state as the terminal motion during free flight. Note that the distinction between the two unstable equilibria is inconsequential in the sense that in either case the free-flight system veers away and displays some other dynamics. Static instability is “obvious” in the sense that it would be apparent even in the setting of a wind tunnel where a single degree of freedom (e.g. attack angle) is statically perturbed and the measured response (pitch moment or torque) found to be destabilizing rather than restorative. In contrast, dynamic instability is the more subtle or “hidden” type that necessarily involves the free-flight couplings among multiple degrees of freedom.

In what follows, we will chart out the stability of equilibria across wide ranges of the input parameters. Throughout these extensive investigations, we have spot-checked many cases by comparing the predictions of the linear analysis against numerical solutions of the full nonlinear model. The two always match. That is, conditions predicted to be linearly stable yield steady motion as the long-time numerical solution to the full model; dynamically unstable but statically stable equilibria yield purely oscillatory instabilities that manifest as growing fluctuations at short times; and statically unstable equilibria, which necessarily have at least one divergent mode and may also have an oscillatory mode or modes, veer away from the equilibrium continuously or with oscillations depending on the dominant eigenmode. This correspondence of the linear analysis with the short-time behavior of the nonlinear system near equilibria is expected for smooth (i.e.  $C^\infty$ ) dynamical systems per the Hartman-Grobman theorem (Strogatz 2018; Hartman 1960, 2002).

### 6.1. Overview of the flight space

The stability map of solutions across the 4-dimensional input parameter space  $(\alpha, W, M, I)$  can be visualized by taking 3D sections in which one quantity is fixed. Figure 9 shows 3D maps in terms of  $(\ell_{CE}, W, M)$ , where the corresponding  $\ell_{CE}(\alpha)$  is displayed as an axis variable in place of  $\alpha$  and where the moment of inertia  $I$  is fixed within each panel and increases across the panels. The chosen values of  $I = 0.01, 1$  and  $10$  are representative of low, intermediate, and high moments of inertia. Each point in the space corresponds to at least one equilibrium according to the preceding existence argument. Unstable equilibria are unmarked and thus correspond to the regions of white space in the plot boxes. Stable equilibria are marked with points whose color denote the angle of attack  $\alpha$ , as specified by the color bar. The axis range  $\ell_{CE} \in [0, 0.3]$  directly reflects the range for the  $\ell_{CP}(\alpha)$  curve (figure 6b) and the equilibrium condition  $\ell_{CE} = \ell_{CP}$ , and no gliding/pancaking states appear outside this range. The interval  $W \in (0, 1)$  is intrinsic to the problem of a dense object in a less dense medium. The range  $M \in (0, 10]$  is truncated at its upper bound only for convenience of plotting, and the solution space continues upwards for larger  $M$  but with no significant change in structure.

From the 3D sections of figure 9, it is clear that the available locations in parameter space for stable systems have a complex structure. Stable gliding may be achieved for greatly different values of any given parameter. There are significant and unique dependencies with respect to all parameters, indicating that all play essential roles in the stability. Surprisingly, the flight stability demonstrates independent behavior with respect to  $W$  and  $M$ , these two respectively encoding the gravitational and inertial aspects of mass. The stable regions appear variously as 3D blobs and quasi-2D sheets, and these may be distinctly separated at places and bridged

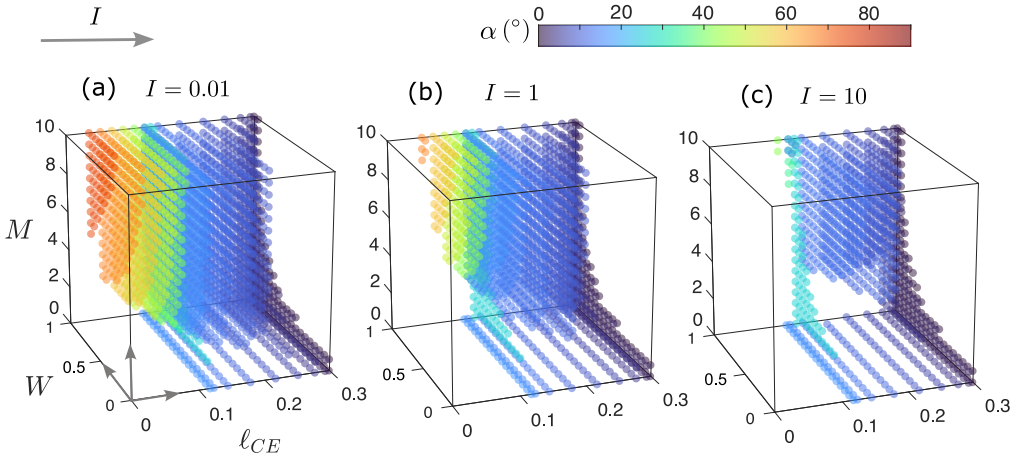


Figure 9: Overview of the 4D parameter space relevant to gliding and pancaking equilibria. Each plot shows the 3D space of the dimensionless parameters ( $\ell_{CE}$ ,  $W$ ,  $M$ ) for fixed values of  $I$ : (a) 0.01, (b) 1, and (c) 10. Each point in the space represents at least one equilibrium. Stable equilibria are indicated with markers colored by the attack angle  $\alpha$  whereas unstable equilibria are left blank.

by quasi-1D filaments elsewhere. A tour through this space reveals some observations and trends that further emphasize this complexity:

- Across the entire space, pancaking with  $\alpha = 90^\circ$  and thus  $\ell_{CE} = 0$  is always unstable. This corresponds to the white space seen in each panel of figure 9 that covers the left coordinate plane. Systems in the near vicinity with low  $\ell_{CE}$  also tend to be unstable, as indicated by the voids on the left sides of each panel. Falling plates thus have an aerodynamic aversion to broadside-on motions.

- For the low  $I \ll 1$  case represented by figure 9a, stable gliding is realized across a wide range of  $\alpha$ , including high- $\alpha$  gliding for high  $M$  and low  $\ell_{CE}$  (red markers). Comparison across the panels shows that the availability of such motions decreases with increasing  $I$ .

- For the moderate  $I = O(1)$  case represented by figure 9b, the central blob of stable solutions shrinks somewhat. Correspondingly, stable gliding is accessible only for low to moderate values of  $\alpha$ . This case also makes more clear the structure for low  $M \ll 1$ , for which stable gliding at low  $\alpha$  is available for approximately  $\ell_{CE} \in [0.1, 0.3]$  and across all  $W \in (0, 1)$ . This planar region of stability lies on the lower coordinate plane or floor of the space, and it is present for all  $I$ .

- For the high  $I \gg 1$  case represented by figure 9c, the central blob shrinks further and stable solutions are confined to a yet lower range of  $\alpha$ . The low- $M$  stable region along the floor is yet more visible, and it is connected to the blob through a vertical filament that seems present for all  $I$ . Also more clear is a set of solutions of very small  $\alpha$  (dark blue) that lies along the right wall or coordinate plane defined by  $\ell_{CE} = 0.3$  and which exists for all  $I$ .

## 6.2. Two-dimensional dissections of the flight space

The space can be further dissected into 2D slices that are more easily displayed and examined. In the tableaux of figures 10 and 11, we investigate the parameter space by taking several 2D slices at fixed  $M$  and  $I$ . The values of  $M = 0.01, 1, 10$  are shown in increasing order downward through the panels, and the values  $I = 0.01, 1, 10$  increase across the panels. These sections are representative of low, moderate, and high cases in each variable, and there are no significant structural changes outside the displayed ranges. The miniature 3D diagram at

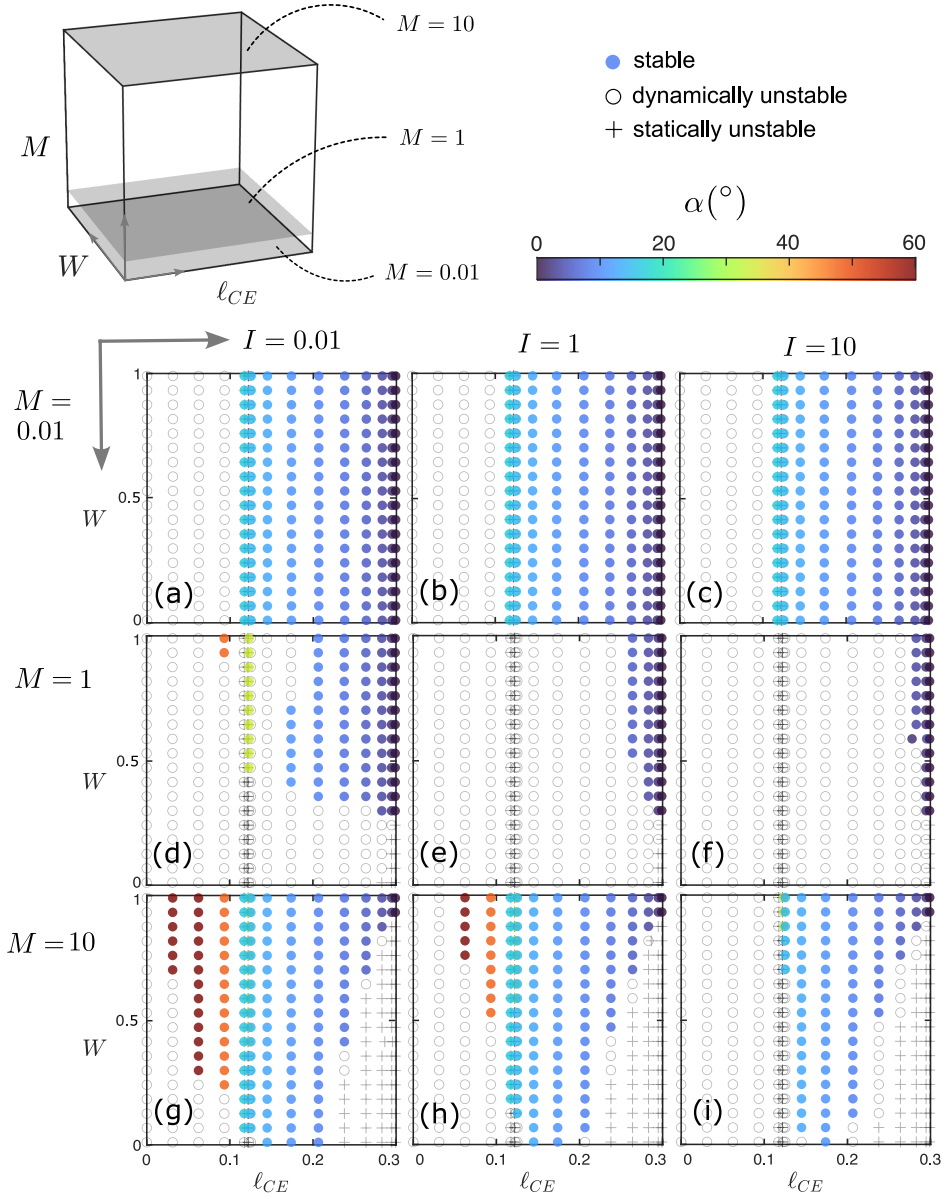


Figure 10: Matrix of 2D sections in the parameters  $(\ell_{CE}, W)$  for fixed  $M$  and  $I$  representing low, moderate and high values. The top left schematic shows the how the 2D sections relate to the 3D plots of figure 9. Stable states are shown with markers colored by the attack angle whereas dynamically and statically unstable equilibria are shown with grey  $\circ$  and  $+$  markers, respectively. The values of  $(M, I)$  are: (a) (0.01, 0.01); (b) (0.01, 1); (c) (0.01, 10); (d) (1, 0.01); (e) (1, 1); (f) (1, 10); (g) (10, 0.01); (h) (10, 1); (i) (10, 10).

the top of figure 10 serves as a guide showing how the 2D slices relate to the 3D diagrams of figure 9. Figures 10 and 11 represent the same information, the former using  $\ell_{CE}$  as an axis variable and  $\alpha$  as the marker color for stable equilibria, and vice versa for the latter. Unstable equilibria of both types are shown as grey markers, where open circles represent

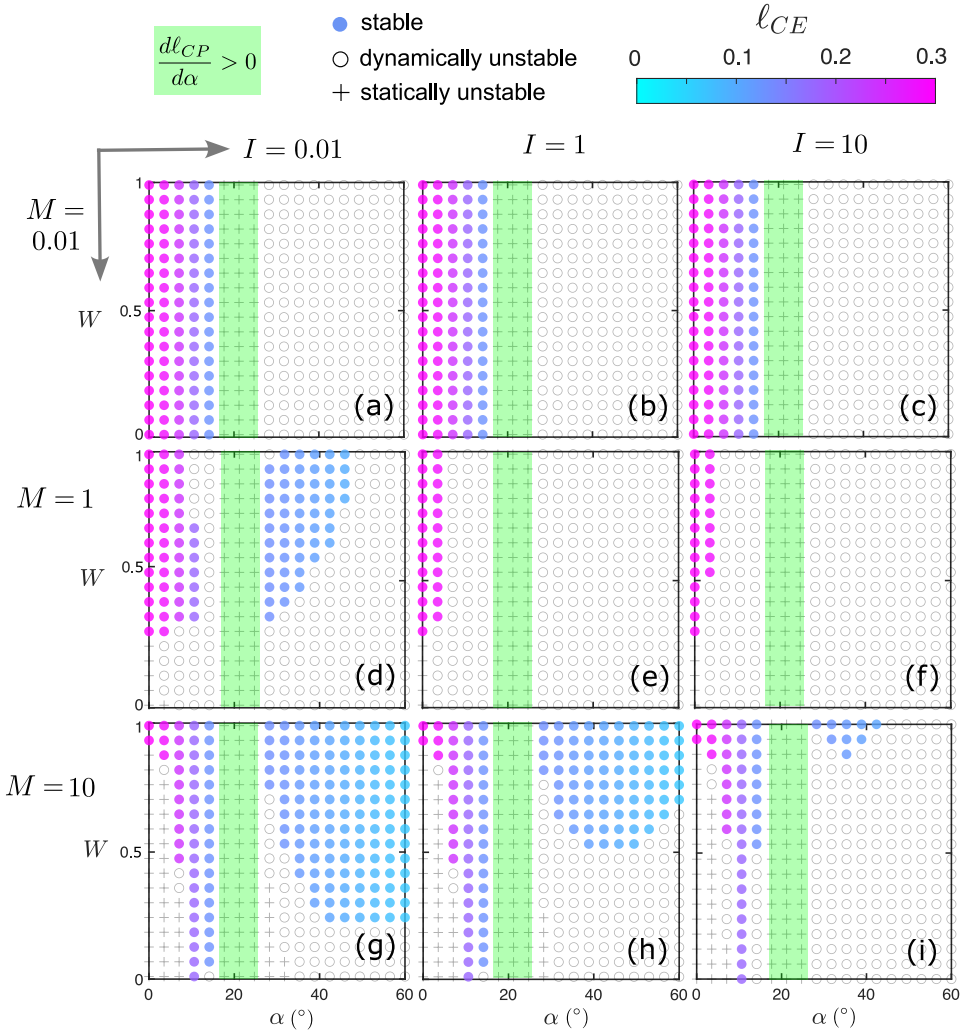


Figure 11: Matrix of 2D sections in the parameters  $(\alpha, W)$  for fixed  $M$  and  $I$  representing low, moderate and high values. This information recasts that of figure 10 so that  $\alpha$  is an axis variable and the corresponding  $\ell_{CE} = \ell_{CP}(\alpha)$  colors the stable states. Dynamically and statically unstable equilibria are again shown with grey  $\circ$  and  $+$  markers, respectively. Those equilibria with  $d\ell_{CP}/d\alpha > 0$  (green shading) are statically unstable. The values of  $(M, I)$  are: (a) (0.01, 0.01); (b) (0.01, 1); (c) (0.01, 10); (d) (1, 0.01); (e) (1, 1); (f) (1, 10); (g) (10, 0.01); (h) (10, 1); (i) (10, 10).

dynamically unstable equilibria and crosses represent statically unstable equilibria. These collectively correspond to the white space in figure 9.

These findings reinforce many of the main messages from the 3D diagrams, notably that pancaking is always unstable while a rich variety of gliding motions are available for different combinations of parameter values. The 2D slices also provide deeper insights into the structure, dependencies and trends and especially additional information about the regimes for differing  $M$ :

- Equilibrium solutions are unique with respect to  $\alpha$  (figure 11) but not unique with respect to  $\ell_{CE}$  (figure 10), which is readily explained by the equilibrium condition  $\ell_{CE} = \ell_{CP}$  and the nonmonotonic form of  $\ell_{CP}(\alpha)$ , as shown in figure 6b. As such, any given location in

the panels of figure 10 may have overlapping points that represent multiple equilibria, some of which may be stable and others unstable. Such cases occur near  $\ell_{CE} \approx 0.12$ . Examples include panel (d) at high  $W$ , where stable gliding equilibria with  $\alpha \approx 35^\circ$  (yellow points) appear together with dynamically and statically unstable equilibria (circles and crosses visible beneath the yellow points). At a similar location in panel (g), two stable gliding equilibria (blue and yellow points) overlap with statically unstable equilibria (crosses).

- For the low  $M \ll 1$  case represented by panels (a-c) in figures 10 and 11, stable gliding is generally available and its structure is simple. The maps are identical and thus independent of  $I$ , and the stability structure is also independent of  $W$ . The region over which stable gliding can be achieved is thus given by the approximate condition  $\ell_{CE} \in (0.12, 0.3)$  or equivalently,  $\alpha \in (0^\circ, 17^\circ)$ .

- For the moderate  $M = O(1)$  case represented by panels (d-f), stable gliding equilibria are generally sparse and especially so for moderate and high  $I$ . For low  $I$  as documented in panel (d), the stable regions appear as two islands separated by unstable equilibria.

- For the high  $M \gg 1$  case represented by panels (g-i), stable gliding is generally available for low  $I$  and less so with increasing  $I$ . The low- $\ell_{CE}$ , high- $\alpha$  stable equilibria are increasingly cut off as  $I$  increases.

### 6.3. Role of center of pressure in gliding stability

The complex structure of the 4D flight space reflects the fact that the eigenvalues and associated stability conditions lack simple mathematical formulas. Nonetheless, our characterizations reveal tidy relationships linking the center of pressure to stability that, while defying analytical derivations, are documented to exactly hold across the entire space of parameters. Specifically, we observe two relations involving the sign of the derivative of  $\ell_{CP}(\alpha)$  or slope of the curve given in figure 6b:

$$\text{stable gliding} \Rightarrow \frac{d\ell_{CP}}{d\alpha} < 0 \quad \text{and} \quad \frac{d\ell_{CP}}{d\alpha} > 0 \Rightarrow \text{statically unstable} \quad (6.1)$$

The first assertion is that all stable gliding solutions have negative pressure center slope. The converse is not true, and there are many cases of negatively sloping  $\ell_{CP}(\alpha)$  that are unstable. Hence, negative slope is a necessary but not sufficient condition for stability. The second assertion is that all equilibria associated with positive slope of the pressure center undergo static instability. The converse is again not true, and there are many statically unstable equilibria with negative slope. The second relation is visually confirmed by comparing figure 6b, where negative slopes are seen for  $\alpha \in (17^\circ, 26^\circ)$ , and figure 11, where the corresponding equilibria are highlighted in green and seen to be unanimously statically unstable (+ markers). Thus, gliding at any angle in this range is strictly forbidden as a free-flight stable state.

These observations connect to the flight dynamical notion of static (in)stability as pertaining to the torque response for a static perturbation to the attack angle in a wind tunnel setting (Etkin & Reid 1995; Anderson 2011; Amin *et al.* 2019). Positive slope  $d\ell_{CP}/d\alpha > 0$  means that the center of pressure moves forward on the wing for a nose-up change in  $\alpha$ , which is destabilizing. So too is the center moving back on the wing in response to a nose-down perturbation. Stable gliding therefore necessarily requires  $d\ell_{CP}/d\alpha < 0$ , though this one condition alone is not sufficient to guarantee stability in free flight where all degrees of freedom participate.

### 6.4. Numerical investigations into unsteady flight states resulting from unstable equilibria

The analysis presented above identifies vast regions of parameter space where flight is unstable, which correspond to the voids in figure 9 and grey markers in figures 10 and 11. It is for these cases that the full nonlinear model yields unsteady flight motions as its numerical



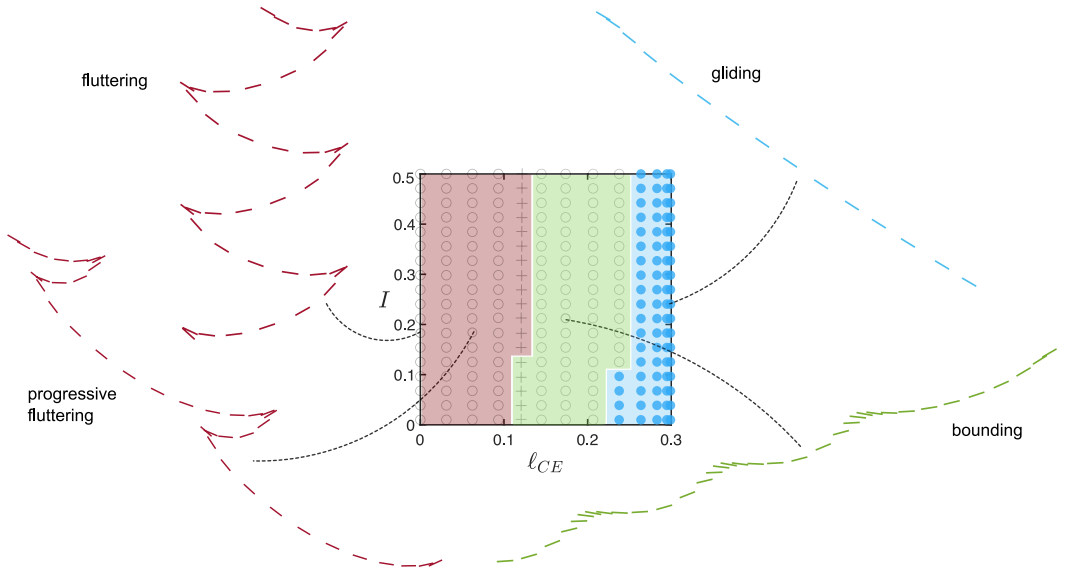


Figure 12: Validation of the model against the experiments of Li *et al.* (2022) whose conditions correspond to varying  $(l_{CE}, I)$  for fixed  $(W, M) = (0.2, 0.14)$ . The four experimentally observed states of fluttering, progressive fluttering, bounding and gliding are reproduced by the model, whose output plate dynamics are shown. The shading delineates the state regimes determined by simulation runs across the 2D parameter space.

solutions. In this section, we extend the survey of such motions presented in section 4.3 and figure 7 and delve deeper into cases of interest. We focus on several 2D sections of the flight space and show that our model successfully reproduces states observed in previous studies and also predicts new free-flight patterns in heretofore unexplored regions of the parameter space.

A first case involves comparisons to the modeling and experimental results of Li *et al.* (2022) on the flight behaviors displayed by plates with displaced centers of mass. In particular, this earlier work reported on fixed values of  $M = 0.14$  and  $W = 0.2$ , for which different unsteady flight states were identified for differing values of  $l_{CE}$  and  $I$ . The modifications in our model relative to that of Li *et al.* (2022) prove to be inconsequential with respect to these results, all of which are faithfully reproduced. In figure 12, we display the relevant region in a 2D slice of parameter space with coloring that denotes 4 unsteady states: fluttering with symmetric back-and-forth swoops, progressive fluttering with asymmetric swoops, bounding with one-way swoops, and steady gliding. The 4 displayed plate motions are numerical solutions to our nonlinear model corresponding to the parameters explored in Li *et al.* (2022). These results confirm the stability type in all cases. Further explorations show these states to be generally available, as indicated by shaded regions identified by running simulations across the ranges  $l_{CE} \in [0, 0.3]$  and  $I \in (0, 0.5]$ . The state boundaries are largely dictated by the former and have weaker dependence on the latter.

Bounding (shown in green in figure 12) is a limit-cycle state that superficially resembles the phugoid motion of aircraft (Montalvo & Costello 2015) but which differs in that the angle of attack increases significantly in what look like approaches to stalling. Such behavior was previously documented for plates with displaced center of mass (Li *et al.* 2022). Bounding occurs for parameters near the stable-unstable border with gliding, and this structure is consistent with a Hopf bifurcation (Guckenheimer & Holmes 2013).

Irregular and aperiodic motions which involve elements of familiar tumbling and fluttering



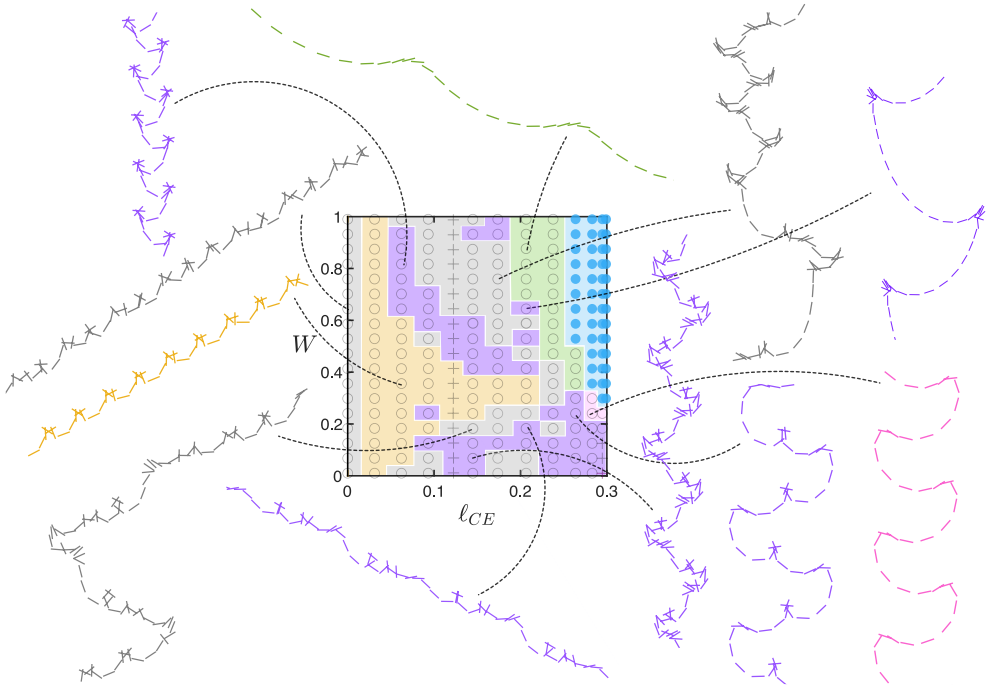


Figure 13: Complex and varied motions dominate for intermediate values of the inertial parameters  $(M, I) = (1, 1)$  where gliding is significantly depleted. This panel repeats figure 10e and adds shading whose different colors indicate the flight states observed in simulation runs across the space. The motions include familiar states such as gliding (blue), bounding (green), meandering (pink) and tumbling (yellow) but also many other periodic states (purple) of varied forms as well as aperiodic and apparently chaotic states (grey).

motions are reported by Andersen *et al.* (2005a) and Hu & Wang (2014) for moderate  $M = O(1)$  and  $I = O(1)$ . Our model reproduces these motions in this intermediate inertial regime, where gliding availability is significantly depleted and a significant majority of equilibria are unstable. In figure 13, whose map is that of figure 10e which has  $(M, I) = (1, 1)$ , we systematically chart the numerical solutions to the nonlinear model for each of the unstable equilibria by shading the state space according to associated long-term flight patterns. The regions are blotchy and irregular, with complex boundaries and islands demarcating the various states. In grey we shade aperiodic and apparently chaotic states, which display no discernible pattern over any timescale; in yellow we shade tumbling; in pink we shade meandering, which is a heretofore unreported flight state described in greater detail in section 7.4; in green we shade bounding; and in light blue we shade stable gliding. In purple we shade those regions which admit periodic hybrid motions that combine multiple characteristics of tumbling, fluttering, meandering, and bounding. Regions of these irregular motions appear in a highly complex fashion in the state space, and more intricate boundaries may exist at a finer resolution of the space than is explored here.

Pancaking or broadside-on falling of a symmetric plate has been reported by Andersen *et al.* (2005a), who found the motion unstable for any  $I$  under the  $Re$  conditions assumed in this work. We report that indeed, pancaking is dynamically unstable for any set of parameters. In figure 14, we hold  $W = 0.8$  and  $\ell_{CE} = 0$  fixed and systematically chart the numerical solutions to the nonlinear model for each of the unstable equilibria by shading the  $(M, I)$  state space according to associated long-term flight patterns. All equilibria are open  $\circ$  markers, and

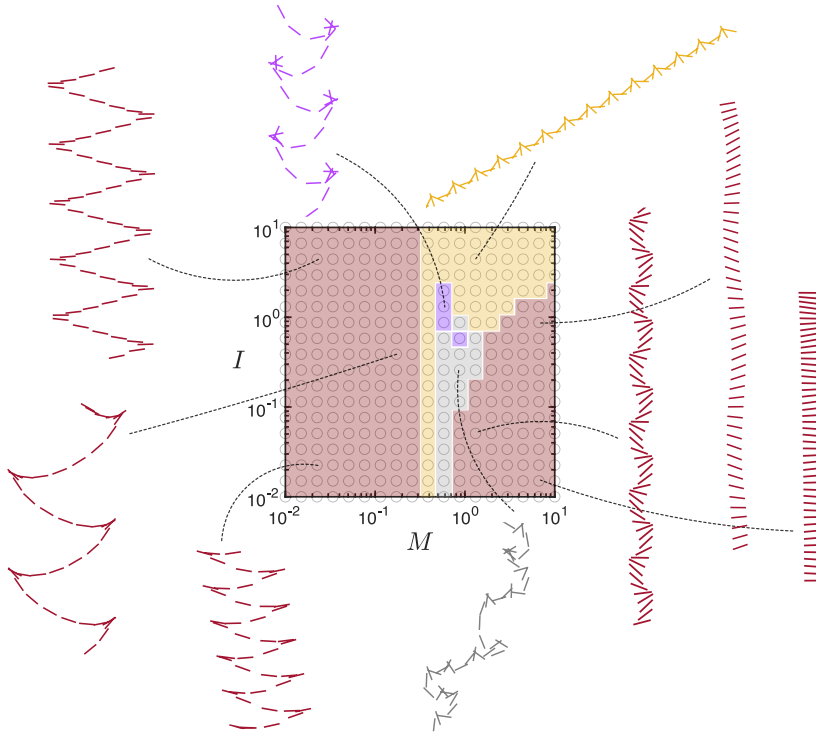


Figure 14: Pancaking is dynamically unstable ( $\circ$ ) for all conditions. For fixed  $(\ell_{CE}, W) = (0, 0.8)$ , the parameters  $(M, I)$  are varied logarithmically to explore the space broadly. The shading indicates the flight state observed in simulations, and example trajectories are displayed. The motions are predominantly forms of fluttering (red) and tumbling (yellow) but with additional periodic (purple) and aperiodic (grey) states occurring for intermediate  $M$  and low to intermediate  $I$ .

so pancaking is always statically stable but dynamically unstable. This figure is representative of any choice of  $W$ , since by equations 4.5,  $W$  drops out for  $\ell_{CE} = 0$ . We plot the information here on a logarithmic scale to better interrogate the intermediate inertial regime where irregular motions abound. In red we shade those regions which display fluttering, and show several different types of fluttering ranging from very weak (right) to very strong (left). As in figure 13, we shade tumbling, aperiodic states, and periodic hybrid states using yellow, grey, and purple, respectively.

## 7. Stability of diving states

We separately assess diving states, which involve edgewise downward descent as depicted in figure 5b. Recalling the arguments of section 3 and the analytical expressions for equilibria of section 5, there are two possible diving postures: a bottom-heavy configuration with the center of equilibrium displaced towards the leading edge side ( $\alpha = 0 = 0^\circ$ ) and a top-heavy configuration with  $\ell_{CE} > 0$  displaced towards the trailing edge ( $\alpha = -\pi = -180^\circ$ ). As expected intuitively, the latter is statically unstable for all parameter values, so throughout this section we focus on the former. We may treat all cases of interest  $\ell_{CE} \geq 0$ , including the symmetric plate of  $\ell_{CE} = 0$  which is degenerate with respect to the two diving postures. As we have shown, diving is distinguished from gliding in that  $\ell_{CE}$  is free since the center of pressure constraint is inoperative. We therefore modify the MATLAB code for stability

analysis of the ODE system 4.5 by supplying  $\ell_{CE}$  as an input for fixed  $\alpha = 0$ . We otherwise use the same classification scheme as in the gliding case:

$$(\ell_{CE}, W, M, I) \Rightarrow (\theta, \vec{v}) \Rightarrow \lambda_i \Rightarrow \begin{cases} \text{stable} & \forall i, \text{Re}(\lambda_i) < 0 \\ \text{statically unstable} & \exists i \text{ s.t. } \text{Re}(\lambda_i) > 0, \text{Im}(\lambda_i) = 0 \\ \text{dynamically unstable} & \text{otherwise} \end{cases}$$

This yields a map from the 4-dimensional input space  $(\ell_{CE}, W, M, I)$  to an output characterization that assumes one of the three stability classifications. The following investigations into diving stability parallel those for gliding.

### 7.1. Overview of the flight space

The 4-dimensional input parameter space  $(\ell_{CE}, W, M, I)$  for diving may be visualized by taking 3D sections in which one quantity is fixed. Figure 15 shows such a 3D space of  $(\ell_{CE}, W, M)$  with the moment of inertia  $I = 1$  fixed at a representative intermediate value. Stable equilibria are marked with colored points, which are uniformly blue to indicate that  $\alpha = 0$  for all. Each such point corresponds to exactly one equilibrium according to the preceding existence and uniqueness arguments. Unstable equilibria are unmarked and thus correspond to the blank spaces in the plot box.

The displayed axis range is  $\ell_{CE} \in [0, 1.5]$ , and there is no significant change in structure for yet greater values. Note that this range extends beyond that for gliding, reflecting that  $\ell_{CE}$  is a free parameter no longer constrained by  $\ell_{CP} \in [0, 0.3]$ . As for gliding, the interval  $W \in (0, 1)$  is intrinsic to the problem. The range  $M \in (0, 10]$  is truncated at its upper bound only for the convenience of plotting, and there is no change in structure for yet greater values. Also shown are two surfaces  $\ell_{CE} = \ell_{CP}(\alpha = 0) = 0.3$  (orange upright plane) and  $\ell_{CM} = W\ell_{CE} = \ell_{CP}(\alpha = 0) = 0.3$  (green hyperbolic sheet) which correspond to some stability boundaries, as discussed further below.

From figure 15, it is clear that the available regions of parameter space for stable diving solutions have a simple structure composed of two distinct but connected regions:

- For low  $M < 1$ , there exists a quasi-planar or sheet-like region where diving is stable for all  $\ell_{CE} > 0.3$  regardless of  $W$ . This forms the floor of the flight space, and it is bounded on one side by the orange surface.
- For high  $M > 1$ , there exists a 3D region bounded by the curved upright wall (green surface). Here, stable diving involves conditions on both  $\ell_{CE}$  and  $W$ .

### 7.2. Two-dimensional dissections of the flight space

More refined insights come from taking 2D sections of the flight space. In the tableau of figure 16, we show slices of  $(\ell_{CE}, W)$  across representative low, moderate, and high values of  $M$  and  $I$ . Here the plot markers again indicate stability status with blue filled markers for stable equilibria, crosses for statically unstable equilibria, and open circles for dynamically unstable equilibria. The latter two unstable cases correspond to the white space in figure 15. These data reinforce the messages distilled from the 3D space and add more details:

- There is exceedingly little variation with the moment of inertia  $I$ . Changes with  $I$  are not altogether absent but they are few and limited to the borders representing transitions between stability and instability or between static and dynamic instabilities. As examples, one may closely compare panels (d) and (e) in the vicinity of  $(\ell_{CE}, W) = (0.4, 0.1)$ .
- Sufficiently low  $\ell_{CE} < \ell_{CP}(\alpha = 0) = 0.3$  is always statically unstable across all values of  $(W, M, I)$ . Note that, strictly speaking, the center of pressure is undefined at  $\alpha = 0$  (figure 6b) and hence should be understood here in the limiting sense. This result means that the plate must be sufficiently front weighted to have a chance of being stable in diving. The

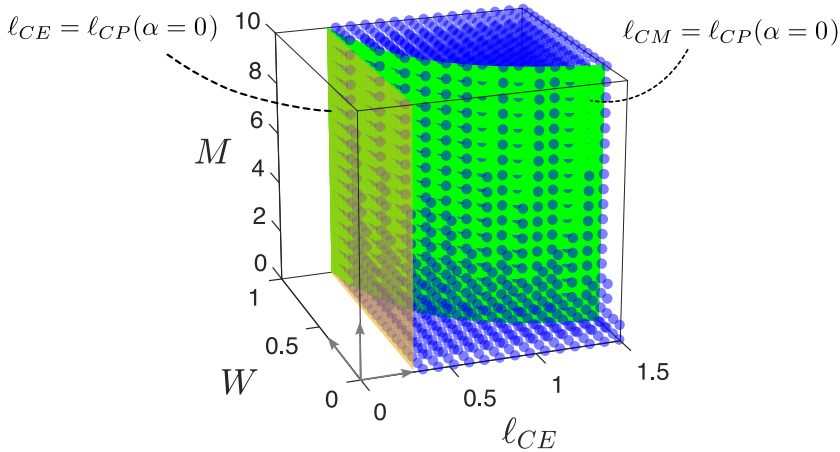


Figure 15: Diving stability ascribes to a simple structure in the parameter space, shown here across varying  $(\ell_{CE}, W, M)$  for a representative value of  $I = 1$ . Each point represents a unique equilibrium that is either stable (blue markers) or unstable (blank). The surfaces  $\ell_{CE} = \ell_{CP}(\alpha = 0) = 0.3$  (orange) and  $\ell_{CM} = W\ell_{CE} = \ell_{CP}(\alpha = 0) = 0.3$  (green) demarcate stability boundaries in different regimes of  $M$ .

relevant boundary is the orange vertical line in each panel, which corresponds to the section through the orange upright plane in figure 15.

- For low mass represented by  $M = 0.1$  in panels (a-c), the simple condition  $\ell_{CE} > \ell_{CP}(\alpha = 0) = 0.3$  seems necessary and sufficient for stable diving. This boundary is shown in all panels as the orange vertical line.

- For moderate mass represented by  $M = 1$  in panels (d-f),  $\ell_{CE}$  must be yet greater to ensure stability when  $W$  is low. Those unstable solutions with  $\ell_{CE} > \ell_{CP}(\alpha = 0) = 0.3$  are mostly but not exclusively of the static-stable but dynamic-unstable type, meaning they will destabilize via growing oscillations.

- For high mass represented by  $M = 10$  in panels (g-i), the simple condition  $\ell_{CM} = W\ell_{CE} > \ell_{CP}(\alpha = 0) = 0.3$  seems necessary and sufficient for stable diving. This boundary is shown as the green hyperbolic curve in each panel, which is the section through the green hyperbolic surface in figure 15. For high mass, dynamically unstable equilibria tend to hug closely the boundary, and the unstable equilibria are otherwise of the static type.

Regarding the near independence of stability status on  $I$ , we lack an explanation for this fact. The mathematical expressions for stability conditions do indeed contain this parameter but it apparently has exceedingly weak effect. Perhaps analysis of the expressions for the eigenvalues could give insight. Regarding the transition in stability status with  $M$ , we discuss some interpretations in what follows.

### 7.3. The roles of the centers of pressure, equilibrium, and mass in diving stability

The above results can be summarized by the following conditions for dynamic stability:

$$\begin{aligned} \text{stable diving at low } M \ll 1 &\iff \ell_{CE} > \ell_{CP}(\alpha = 0) = 0.3 \quad \text{and} \\ \text{stable diving at high } M \gg 1 &\iff \ell_{CM} = W\ell_{CE} > \ell_{CP}(\alpha = 0) = 0.3 \end{aligned} \quad (7.1)$$

The two-way arrows indicate necessary and sufficient relations. In words, low-mass stable diving requires the center of equilibrium to be forward of the center of pressure, and high-mass stable diving requires the center of mass to be forward of the center of pressure. These outcomes are empirically validated but we lack proofs, and so the above claims should be

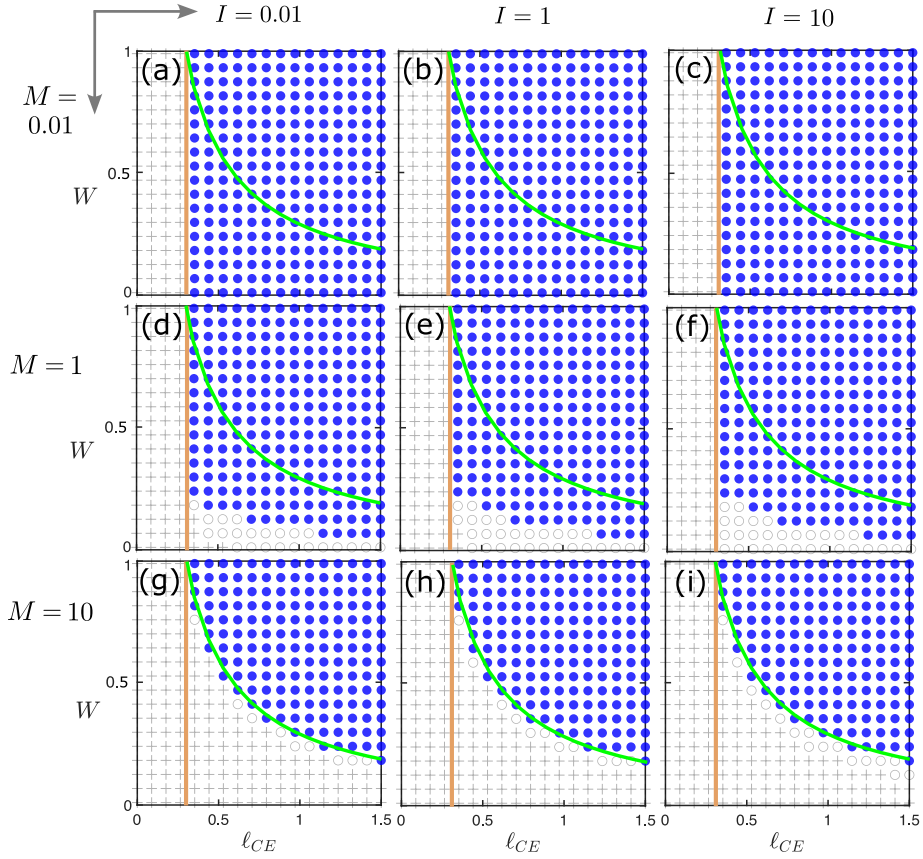


Figure 16: Matrix of 2D sections in the parameters  $(\ell_{CE}, W)$  for fixed  $M$  and  $I$  representing low, moderate and high values. The middle column with  $I = 1$  represents constant- $M$  sections of figure 15. Stable diving states are shown as blue markers whereas dynamically and statically unstable equilibria are shown with grey  $\circ$  and  $+$  markers, respectively. The orange and green curves are sections through the corresponding surfaces of figure 15 and which are important stability boundaries in the limits of low and high mass. The values of  $(M, I)$  are: (a) (0.01, 0.01); (b) (0.01, 1); (c) (0.01, 10); (d) (1, 0.01); (e) (1, 1); (f) (1, 10); (g) (10, 0.01); (h) (10, 1); (i) (10, 10).

viewed as conjectures that are empirically validated here across wide ranging conditions. Future work may pursue derivations by analyzing the eigenvalues in the appropriate limits.

Intuitively, these conditions state that plates must be weighted sufficiently forward for stable diving. This seems to relate to the directional or yaw stability of aircraft, which presumably have  $M \gg 1$ . For this so-called weathervane effect, the center of mass is viewed as a pivot point that must be sufficiently forward of the vertical stabilizer on the tail where pressure forces act (Anderson & Bowden 2005), which is consistent with the second condition given above. Our findings are also quantitatively consistent with the experiments of Li *et al.* (2022) involving flight tests in water of plastic plates to which weights were added to displace the centers of mass and equilibrium. Here the low relative mass  $M = 0.14$  means the first condition applies, and indeed the observation by Li *et al.* (2022) that diving occurs only for  $\ell_{CE} > 0.3$  aligns with our findings.

Less intuitive is that different regimes of  $M$  involve different specifications of what exactly constitutes sufficient front weighting, one case involving  $\ell_{CE}$  and the other  $\ell_{CM}$ . This

indicates that the two factors play distinct roles, defying the intuition that the former is simply a generalization of the latter in situations in which buoyancy is a factor. Similarly, the inertial and gravitational aspects of mass play different roles, with  $M$  dictating which condition is applicable and  $W$  appearing within one of the conditional statements. Better understanding the origin of these subtleties is an avenue for future work. Our preliminary investigations show that the newly added torque from rotational lift  $\tau_{RL}$  is in general an important determinant for diving stability. Without such a term, the model reverts to that of Li *et al.* (2022), whose stability maps differ substantially in the regime of high  $M$ . Namely, the stable region is then  $\ell_{CE} \in (\ell_{CP}, \ell_{CP}/W)$ , which lies between the orange and green curves in the sections of figure 16g-i. This seems implausible in that strongly front-weighted plates are predicted to be unstable. Future experiments would provide valuable information that would distinguish the models and perhaps further inform on the role of  $\tau_{RL}$  and its mathematical form.

#### 7.4. Meandering: a new unsteady flight state

Our investigations into the stability of diving reveal an unsteady state which has not to our knowledge been documented in previous studies. We call such behavior *meandering*, which consists of smoothly waving side-to-side excursions during descent. Example trajectories are shown in pink in figures 7 and 13. The main characteristics of this new class of motions include:

- Meandering, like fluttering, involves periodic back-and-forth oscillations about a directly downward trajectory. Whereas fluttering has sharply cusped reversals during which the plate does not flip over, meandering involves smooth turns during which the plate inverts in the sense of which face is projected upwards. Mathematically, the distinction is that  $\hat{y}' \cdot \hat{y}$  is single-signed for fluttering but alternates in sign for meandering.
- Meandering can originate as an instability of low- $\alpha$  gliding. Examples are shown on the left of figure 17, for which the map repeats that of figure 10h with  $M = 10$  and  $I = 1$ . The light blue points are uniformly colored here to indicate stable gliding regardless of attack angle, and a corresponding stable gliding trajectory is shown ( $\ell_{CE} = 0.15$ , light blue). Meandering states (pink) arise as  $\ell_{CE}$  is increased, and this appearance of a limit cycle state near a stability border is consistent with a supercritical Hopf bifurcation (Guckenheimer & Holmes 2013). The side-to-side excursion amplitude for meandering is highest for those states nearest the gliding stability boundary, i.e. for  $\ell_{CE}$  closer to the plate center.
- Meandering can also arise as an instability of diving, which parallels how fluttering emerges in a similar way from pancaking. Examples are shown on the right of figure 17, for which the map repeats that of figure 16h with  $M = 10$  and  $I = 1$ . Here a stable diving trajectory is shown in blue ( $\ell_{CE} = 1.25$ ). Meandering states (pink) are found at the lower values of  $\ell_{CE}$  corresponding to the region between the orange and green curves. Here again the stability structure is reminiscent of a supercritical Hopf bifurcation, and the excursion amplitude is seen to decrease with increasing  $\ell_{CE}$ .
- The results of figure 17 are typical of  $M \gg 1$ , for which meandering generally arises for those  $\ell_{CE}$  too large to admit stable gliding and yet not sufficiently large to achieve stable diving. This solution can result from the region of instability regardless of static stability (+ markers) or static instability (o). The decreasing amplitude of meandering for increasing  $\ell_{CE}$  can be understood intuitively: cases of low  $\ell_{CE}$  represent failures to glide involving large lateral excursions, whereas cases of higher  $\ell_{CE}$  are failures to dive with small excursions.

Meandering has heretofore been undocumented because the requisite conditions were not explored in previous studies. The work of Li *et al.* (2022) seems to be the only experiments and modeling to address the necessarily large displacements in center of equilibrium  $\ell_{CE} \gtrsim 0.2$ , but the mass  $M \approx 0.1$  was limited to low values for which figure 16a shows the necessary



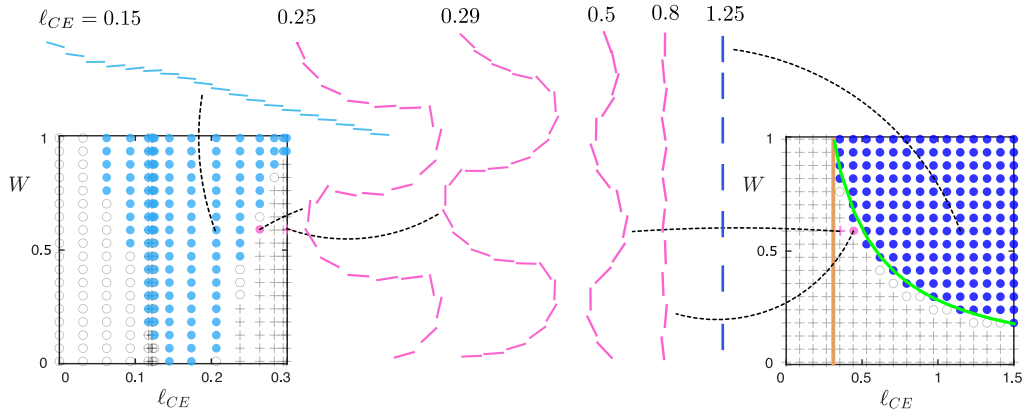


Figure 17: Meandering is a periodic state arising from unstable equilibria between stable gliding and stable diving. The panels represent fixed  $(M, I) = (10, 1)$  and varying  $(\ell_{CE}, W)$  over ranges appropriate to gliding and diving, and they repeat those of figures 11h and 16h. Sample meandering trajectories (pink) of varying horizontal excursion amplitudes are accessed by varying  $\ell_{CE}$  across values between stable gliding (light blue) and stable diving (dark blue).

unstable equilibria for meandering to be absent. Future experiments testing our predictions could use figure 17 as a guide in choosing the relevant parameter values. For example, the case of  $(\ell_{CE}, W, M, I) = (0.25, 0.6, 10, 1)$  yields the high-amplitude meandering, and such conditions should be achievable with strongly front-weighted plates falling in water.

## 8. Discussion and conclusions

This study provides a framework with which to analyze steady gliding and diving motions for a wide array of physical parameters. We introduce dimensionless constants  $(\ell_{CE}, W, M, I)$  that fully describe the plate-fluid system for a passively falling plate. We show that for any choice of these parameters, there exists a unique steady gliding or diving solution. We introduce a dimensionless version of the quasi-steady aerodynamic model developed by Li *et al.* (2022), and modify the treatment of rotational lift to include its contribution to the overall torque on the body. We validate explicitly that the solutions to the equilibrium equations for this model are unique for a given set of parameters  $(\alpha, W, M, I)$ . We then analyze this dimensionless model through a systematic linear stability analysis to reveal a complex set of conditions that govern the stability of gliders and divers, as well as a rich array of available flight states. Finally, we identify a previously-unknown flight pattern, dubbed meandering, that arises out of a stable limit cycle solution between the stability boundaries of gliders and divers.

There are several improvements available for the model introduced in this work. The new term encoding the torque from rotational lift,  $\tau_{RL}$ , uses a zeroth-order guess for a center of rotational lift,  $\ell_{CRL} = 0$  at which the rotational lift effectively acts. This term could be empirically validated or updated. Experiments to confirm the existence of the predicted meandering flight state, and to identify where in parameter space it arises, would also validate the inclusion of this term. In this vein, empirical confirmation of the extremely weak dependence on the moment of inertia  $I$  for diver stability may lend more understanding of this counter-intuitive result. Experimentation to confirm the high- $\alpha$  gliding that is predicted in this work for high  $M$  would also be a good avenue for future work, as the quasi-steady approximation may break down due to flow separation at these high attack angles.



This model is applicable to thin structures at intermediate Reynolds numbers, so it has a broad range of potential uses for a variety of physical systems. The computational tools for analysis introduced here seem necessary to efficiently explore the large parameter space, as a pen-and-paper analysis is not feasible for such a complex set of equations. A major success of this work is that a variety of motions, both steady and unsteady, are predicted across widely ranging parameters. This may open up many applications for motions in air and through water, both in understanding biological locomotion as well as for designing biomimetic flying and swimming vehicles.

**Acknowledgements.** We thank H. Li, C. Mavroyiakoumou, Z. J. Wang and J. Wu for useful discussions.

**Funding.** We acknowledge support from the U.S. National Science Foundation (1847955).

**Declaration of interests.** The authors report no conflict of interest.

**Author ORCIDs.** O. Pomerenk, <https://orcid.org/0000-0002-0481-3952>; L. Ristroph, <https://orcid.org/0000-0001-9358-0689>

**Author contributions.** O.P. and L.R. contributed to all aspects of this work.

## Appendix A.

For the order-1 calculations to produce figure 2, we approximate fliers as systems which have a cylindrical fuselage body of mass  $M$ , length  $L$ , and radius  $R$ , with a thin rectangular wing of thickness  $h$ , chord length  $\ell$ , span length  $s$ , and mass  $m$  cutting through the center of the cylinder (a simple “airplane” structure). The ambient fluid has density  $\rho_f$ . Bodies which may be approximated as just wings, e.g. a piece of paper, have  $M = L = R = 0$ . To calculate dimensionless quantities for this winged cylindrical body system, we compute using table 2 the quantities

$$\begin{aligned} I_{\text{body}} &= \frac{1}{12}M(3R^2 + L^2) \\ I_{\text{wing}} &= \frac{1}{12}m(\ell^2 + h^2) \\ I_{\text{wing (air)}} &= \frac{1}{2}\rho_f\pi s\left(\frac{\ell}{2}\right)^4 \end{aligned} \tag{A 1}$$

where the wing-air moment of inertia is a cylindrical fluid column with  $I = \frac{1}{2}mr^2$ . Then, we compute

$$\begin{aligned} I^* &= \frac{I_{\text{body}} + I_{\text{wing}}}{I_{\text{wing (air)}}} \\ M^* &= \frac{M + m}{\pi\rho_f s\left(\frac{\ell}{2}\right)^2} \\ W &= g(M + m) \\ B &= g\rho_f(s\ell h + \pi R^2 L) \\ W^* &= \frac{W - B}{W}. \end{aligned} \tag{A 2}$$

System	$M$	$m$	$s$	$\ell$	$L$	$R$	$h$	$\rho_f$	Reference
Bird	691	62.1	68	33.5	40	5.5	1	1.2e-3	Berg & Rayner (1995)
Watercraft	60000	20000	120	20	140	12	1	1	Wood & Inzartsev (2009)
Paper in air	0	0.59	15	5.1	0	0	0.01	1.2e-3	Li <i>et al.</i> (2022)
Plastic plate in water	0	9.12	20.3	2.54	0	0	0.15	1	Li <i>et al.</i> (2022)
Stingray	0	8000	60	50	0	0	2	1	Yigin & Ismen (2012)
Metal plate in water	0	8.31	19	1	0	0	0.162	1	Andersen <i>et al.</i> (2005 <i>b</i> )
Flying squirrel	0	70	11	13	0	0	3	1.2e-3	Thorington Jr & Heaney (1981)
Cucumber seed	0	0.21	12	6.2	0	0	0.1	1.2e-3	Viola & Nakayama (2022)
Butterfly	0	2	20	20	0	0	0.005	1.2e-3	Hu & Wang (2010)
Snowflake	0	3.3e-5	0.4	0.4	0	0	0.001	1.2e-3	Langleben (1954)
Marine snow	0	0.0001	0.05	0.05	0	0	0.001	1	Passow <i>et al.</i> (2012)
Scallop	0	100	6	6	0	0	1	1	Cheng <i>et al.</i> (1996)
Flounder	0	2300	30	60	0	0	1	1	Takagi <i>et al.</i> (2010)
Air vehicle	0	0.265	10	1.5	0	0	0.1	1.2e-3	Wood <i>et al.</i> (2007)

Table 2: Systems that may be approximated as winged cylindrical bodies. All units are  $\text{cm} \cdot \text{g}$ . Displayed are  $M$ , mass of the fuselage body;  $m$ , mass of the wing;  $s$ , span length of the plate;  $\ell$ , chord length of the wing;  $L$ , length of the fuselage body;  $R$ , radius of the fuselage body;  $h$ , thickness of the wing; and  $\rho_f$ , density of the fluid.

- AMIN, KHUNSA, HUANG, JINZI MAC, HU, KEVIN J, ZHANG, JUN & RISTROPH, LEIF 2019 The role of shape-dependent flight stability in the origin of oriented meteorites. *Proceedings of the National Academy of Sciences* **116** (33), 16180–16185.
- ANDERSEN, ANDERS, PESAVENTO, UMBERTO & WANG, Z JANE 2005*a* Analysis of transitions between fluttering, tumbling and steady descent of falling cards. *Journal of Fluid Mechanics* **541**, 91–104.
- ANDERSEN, A, PESAVENTO, U & WANG, Z JANE 2005*b* Unsteady aerodynamics of fluttering and tumbling plates. *Journal of Fluid Mechanics* **541**, 65–90.
- ANDERSON, JOHN 2011 *Fundamentals of Aerodynamics*. McGraw Hill.
- ANDERSON, JOHN DAVID & BOWDEN, MARY L 2005 *Introduction to flight*, , vol. 582. McGraw-Hill Higher Education New York, NY, USA.
- BERG, COEN VAN DEN & RAYNER, JEREMY MV 1995 The moment of inertia of bird wings and the inertial power requirement for flapping flight. *Journal of experimental biology* **198** (8), 1655–1664.
- BERGOU, ATTILA J, RISTROPH, LEIF, GUCKENHEIMER, JOHN, COHEN, ITAI & WANG, Z JANE 2010 Fruit flies modulate passive wing pitching to generate in-flight turns. *Physical review letters* **104** (14), 148101.
- BIRCH, JAMES M & DICKINSON, MICHAEL H 2003 The influence of wing–wake interactions on the production of aerodynamic forces in flapping flight. *Journal of experimental biology* **206** (13), 2257–2272.
- CERTINI, DANIELE 2023 The flight of *alsomitra macrocarpa*. PhD thesis, University of Edinburgh.
- CHENG, J-Y, DAVISON, IG & DEMONT, ME 1996 Dynamics and energetics of scallop locomotion. *Journal of Experimental Biology* **199** (9), 1931–1946.
- DICKINSON, MICHAEL H, LEHMANN, FRITZ-OLAF & SANE, SANJAY P 1999 Wing rotation and the aerodynamic basis of insect flight. *science* **284** (5422), 1954–1960.
- DICKSON, WILLIAM B & DICKINSON, MICHAEL H 2004 The effect of advance ratio on the aerodynamics of revolving wings. *Journal of Experimental Biology* **207** (24), 4269–4281.
- ELLINGTON, CHARLES P 1999 The novel aerodynamics of insect flight: applications to micro-air vehicles. *Journal of Experimental Biology* **202** (23), 3439–3448.
- ENNOS, A ROLAND 1989 The effect of size on the optimal shapes of gliding insects and seeds. *Journal of Zoology* **219** (1), 61–69.
- ETKIN, BERNARD & REID, LLOYD DUFF 1995 *Dynamics of flight: stability and control*. John Wiley & Sons.
- FARREN, WILLIAM SCOTT 1935 The reaction on a wing whose angle of incidence is changing rapidly. wind tunnel experiments with a short period recording balance. *Tech. Rep.*. HM Stationery Office.
- FUNG, YUAN CHENG 2008 *An introduction to the theory of aeroelasticity*. Courier Dover Publications.

- GUCKENHEIMER, JOHN & HOLMES, PHILIP 2013 *Nonlinear oscillations, dynamical systems, and bifurcations of vector fields*, vol. 42. Springer Science & Business Media.
- HARTMAN, PHILIP 1960 A lemma in the theory of structural stability of differential equations. *Proceedings of the American Mathematical Society* **11** (4), 610–620.
- HARTMAN, PHILIP 2002 *Ordinary differential equations*. SIAM.
- HU, RUIFENG & WANG, LIFENG 2014 Motion transitions of falling plates via quasisteady aerodynamics. *Physical Review E* **90** (1), 013020.
- HU, YE & WANG, JINJUN 2010 Experimental investigation on aerodynamic performance of gliding butterflies. *AIAA journal* **48** (10), 2454–2457.
- HUANG, WENTAO, LIU, HONG, WANG, FUXIN, WU, JUNQI & ZHANG, HP 2013 Experimental study of a freely falling plate with an inhomogeneous mass distribution. *Physical Review E* **88** (5), 053008.
- JAFFERIS, NOAH T, HELBLING, E FARRELL, KARPELSON, MICHAEL & WOOD, ROBERT J 2019 Untethered flight of an insect-sized flapping-wing microscale aerial vehicle. *Nature* **570** (7762), 491–495.
- KEENNON, MATTHEW, KLINGEBIEL, KARL & WON, HENRY 2012 Development of the nano hummingbird: A tailless flapping wing micro air vehicle. In *50th AIAA aerospace sciences meeting including the new horizons forum and aerospace exposition*, p. 588.
- KRAMER, VON M 1932 Die zunahme des maximalauftriebes von tragflugeln bei plotzlicher anstellwinkelvergrosserung (boeneffekt). *Z. Flugtech. Motorluftschiff* **23**, 185–189.
- LANGLEBEN, MANUEL PHILLIP 1954 The terminal velocity of snowflakes. *Quarterly Journal of the Royal Meteorological Society* **80** (344), 174–181.
- LEE, YJ, LUA, KIM-BOON, LIM, TT & YEO, KS 2016 A quasi-steady aerodynamic model for flapping flight with improved adaptability. *Bioinspiration & biomimetics* **11** (3), 036005.
- LI, HUILIN, GOODWILL, TRISTAN, WANG, Z JANE & RISTROPH, LEIF 2022 Centre of mass location, flight modes, stability and dynamic modelling of gliders. *Journal of Fluid Mechanics* **937**, A6.
- LIU, H 2005 Simulation-based biological fluid dynamics in animal locomotion .
- LOGAN, J DAVID 2013 *Applied mathematics*. John Wiley & Sons.
- MAXWELL, JAMES CLERK 1854 On a particular case of the descent of a heavy body in a resisting medium. *Camb. Dublin Math. J* **9**, 145–148.
- MILLER, LAURA A, GOLDMAN, DANIEL I, HEDRICK, TYSON L, TYTELL, ERIC D, WANG, Z JANE, YEN, JEANNETTE & ALBEN, SILAS 2012 Using computational and mechanical models to study animal locomotion.
- MONTALVO, CARLOS & COSTELLO, MARK 2015 Meta aircraft flight dynamics. *Journal of Aircraft* **52** (1), 107–115.
- MUNK, MAX M 1925 Note on the air forces on a wing caused by pitching. *Tech. Rep.*.
- NAKATA, TOSHIYUKI, LIU, HAO & BOMPHREY, RICHARD J 2015 A cfd-informed quasi-steady model of flapping-wing aerodynamics. *Journal of fluid mechanics* **783**, 323–343.
- PASSOW, UTA, ZIERVOGEL, K, ASPER, V & DIERCKS, A 2012 Marine snow formation in the aftermath of the deepwater horizon oil spill in the gulf of mexico. *Environmental Research Letters* **7** (3), 035301.
- PESAVENTO, UMBERTO 2006 *Unsteady aerodynamics of falling plates*. Cornell University.
- PESAVENTO, UMBERTO & WANG, Z JANE 2004 Falling paper: Navier-stokes solutions, model of fluid forces, and center of mass elevation. *Physical review letters* **93** (14), 144501.
- RISTROPH, LEIF, BERGOU, ATTILA J, GUCKENHEIMER, JOHN, WANG, Z JANE & COHEN, ITAI 2011 Paddling mode of forward flight in insects. *Physical review letters* **106** (17), 178103.
- RISTROPH, LEIF, BERGOU, ATTILA J, RISTROPH, GUNNAR, COUMES, KATHERINE, BERMAN, GORDON J, GUCKENHEIMER, JOHN, WANG, Z JANE & COHEN, ITAI 2010 Discovering the flight autostabilizer of fruit flies by inducing aerial stumbles. *Proceedings of the National Academy of Sciences* **107** (11), 4820–4824.
- RISTROPH, LEIF & CHILDRESS, STEPHEN 2014 Stable hovering of a jellyfish-like flying machine. *Journal of The Royal Society Interface* **11** (92), 20130992.
- RISTROPH, LEIF, RISTROPH, GUNNAR, MOROZOVA, SVETLANA, BERGOU, ATTILA J, CHANG, SONG, GUCKENHEIMER, JOHN, WANG, Z JANE & COHEN, ITAI 2013 Active and passive stabilization of body pitch in insect flight. *Journal of The Royal Society Interface* **10** (85), 20130237.
- SANE, SANJAY P 2003 The aerodynamics of insect flight. *Journal of experimental biology* **206** (23), 4191–4208.
- SANE, SANJAY P & DICKINSON, MICHAEL H 2001 The control of flight force by a flapping wing: lift and drag production. *Journal of experimental biology* **204** (15), 2607–2626.

- SANE, SANJAY P & DICKINSON, MICHAEL H 2002 The aerodynamic effects of wing rotation and a revised quasi-steady model of flapping flight. *Journal of experimental biology* **205** (8), 1087–1096.
- SCHLICHTING, HERMANN & GERSTEN, KLAUS 2016 *Boundary layer theory*. Springer.
- STROGATZ, STEVEN H 2018 *Nonlinear dynamics and chaos with student solutions manual: With applications to physics, biology, chemistry, and engineering*. CRC press.
- SUN, MAO & TANG, JIAN 2002 Unsteady aerodynamic force generation by a model fruit fly wing in flapping motion. *Journal of experimental biology* **205** (1), 55–70.
- TAKAGI, TSUTOMU, KAWABE, RYO, YOSHINO, HIROYUKI & NAITO, YASUHIKO 2010 Functional morphology of the flounder allows stable and efficient gliding: an integrated analysis of swimming behaviour. *Aquatic Biology* **9** (2), 149–153.
- THORINGTON JR, RICHARD W & HEANEY, LAWRENCE R 1981 Body proportions and gliding adaptations of flying squirrels (petauristinae). *Journal of Mammalogy* **62** (1), 101–114.
- TRITTON, DAVID J 2012 *Physical fluid dynamics*. Springer Science & Business Media.
- VIOLA, IGNAZIO MARIA & NAKAYAMA, NAOMI 2022 Flying seeds. *Current Biology* **32** (5), R204–R205.
- WALKER, JEFFREY A 2002 Rotational lift: something different or more of the same? *Journal of Experimental Biology* **205** (24), 3783–3792.
- WANG, QI, GOOSEN, JFL & VAN KEULEN, FRED 2016 A predictive quasi-steady model of aerodynamic loads on flapping wings. *Journal of Fluid Mechanics* **800**, 688–719.
- WANG, QING, HE, KAI-FENG, QIAN, WEI-QI, ZHANG, TIAN-JIAO, CHENG, YAN-QING & WU, KAI-YUAN 2012 Unsteady aerodynamics modeling for flight dynamics application. *Acta Mechanica Sinica* **28**, 14–23.
- WANG, WEI, DAI, XIA, LI, LIANG, GHENETI, BANTI H, DING, YANG, YU, JUNZHI & XIE, GUANGMING 2018 Three-dimensional modeling of a fin-actuated robotic fish with multimodal swimming. *IEEE/ASME Transactions on Mechatronics* **23** (4), 1641–1652.
- WANG, Z JANE 2016 Insect flight: from newton's law to neurons. *Annual Review of Condensed Matter Physics* **7** (1), 281–300.
- WANG, Z JANE, BIRCH, JAMES M & DICKINSON, MICHAEL H 2004 Unsteady forces and flows in low reynolds number hovering flight: two-dimensional computations vs robotic wing experiments. *Journal of Experimental Biology* **207** (3), 449–460.
- WOOD, ROBERT J, AVADHANULA, SRINATH, STELTZ, ERIK, SEEMAN, M, ENTWISTLE, JON, BACHRACH, ABRAHAM, BARROWS, G, SANDERS, SETH & FEAR, RONALD S 2007 An autonomous palm-sized gliding micro air vehicle. *IEEE Robotics & Automation Magazine* **14** (2), 82–91.
- WOOD, STEPHEN & INZARTSEV, AV 2009 *Autonomous underwater gliders*. Citeseer.
- YIGIN, C CIGDEM & ISMEN, ALI 2012 Age, growth and reproduction of the common stingray, *dasyatis pastinaca* from the north aegean sea. *Marine Biology Research* **8** (7), 644–653.